Journal of Medicinal Chemistry

pubs.acs.org/jmc

Article

Copper-Based Complexes with Adamantane Ring-Conjugated *bis*(3,5-Dimethyl-pyrazol-1-yl)acetate Ligand as Promising Agents for the Treatment of Glioblastoma

Maria Beatrice Morelli, Miriam Caviglia, Carlo Santini, Jo' Del Gobbo, Laura Zeppa, Fabio Del Bello,* Gianfabio Giorgioni, Alessandro Piergentili, Wilma Quaglia, Chiara Battocchio,* Federica Bertelà, Simone Amatori, Carlo Meneghini, Giovanna Iucci, Iole Venditti, Alessandro Dolmella, Michele Di Palma, and Maura Pellei

Cite This: https://doi.org/10.1021/acs.jmedchem.4c00821

Read Online

ACCESS | Metrics & More | Article Recommendations | Supporting Information

ABSTRACT: The new ligand L^{2Ad}, obtained by conjugating the bifunctional species bis(3,5-dimethylpyrazol-1-yl)-acetate and the drug amantadine, was used as a chelator for the synthesis of new Cu complexes **1**−**5**. Their structures were investigated by synchrotron radiation-induced X-ray photoelectron spectroscopy (SR-XPS), near-edge X-ray absorption fine structure (NEXAFS) spectroscopy, and by combining X-ray absorption fine structure (XAFS) spectroscopy techniques and DFT modeling. The structure of complex **3** was determined by single-crystal X-ray diffraction analysis. Tested on U87, T98, and U251 glioma cells, Cu(II) complex **3** and Cu(I) complex **5** decreased cell viability with IC_{50} values significantly lower than cisplatin, affecting cell growth, proliferation, and death. Their effects were prevented by treatment with the Cu chelator tetrathiomolybdate, suggesting the involvement of copper in their cytotoxic activity. Both complexes were able to increase ROS production, leading to DNA damage and death. Interestingly, nontoxic doses of **3** or **5** enhanced the chemosensitivity to Temozolomide.

1. INTRODUCTION

Metal-based chemotherapy is a well-established anticancer option.[1] Platinum-based drugs, such as cisplatin, oxaliplatin, and carboplatin, are effective agents widely used in the treatment of several tumors.[2] However, their therapeutic potential is limited by marked side effects and chemo-resistance,[3−5] and bioinorganic research is trying to give new answers to the demand for more efficient metallodrugs. An important field aiming to identify other antitumor-active complexes with better pharmacological profiles and different innovative targets compared to Pt-based drugs concerns the employment of biologically active complexes with essential ions. Indeed, since essential metals escaping their metabolic pathways could be very toxic to the body, complexes of such metals might act as efficacious cytotoxic agents. Copper is one of the essential trace metals for all organisms living in oxygen-rich environments. It plays a crucial role in eukaryotic redox chemistry, growth, and development being a redox catalytic cofactor of different proteins and enzymes involved, among others, in mitochondrial respiration, energy metabolism, collagen cross-linking, antioxidation, and catecholamine biosynthesis.[6] Cu-based complexes have shown interesting antitumor and antimetastatic properties against different types of solid tumors, acting through peculiar mechanisms of action (deoxyribonucleic acid (DNA) damage, reactive oxygen species (ROS) generation, proteasome inhibition, glutathione (GSH) depletion), which are markedly different from those of Pt-based drugs.[7−9] Moreover, since endogenous metal ions generally show toxicity lower than nonendogenous ones against normal cells, copper complexes might be valuable alternatives to Pt-based compounds, allowing them to overcome problems such as inherent or acquired resistance and dose-limiting toxicity.[1,10]

Copper has been reported to play specific roles in the pathophysiology of human brain cancers and deregulation of its metabolism causes toxicity.[11,12] Recently, copper chelators and copper coordination compounds have been demonstrated

Received: April 6, 2024
Revised: May 21, 2024
Accepted: May 24, 2024

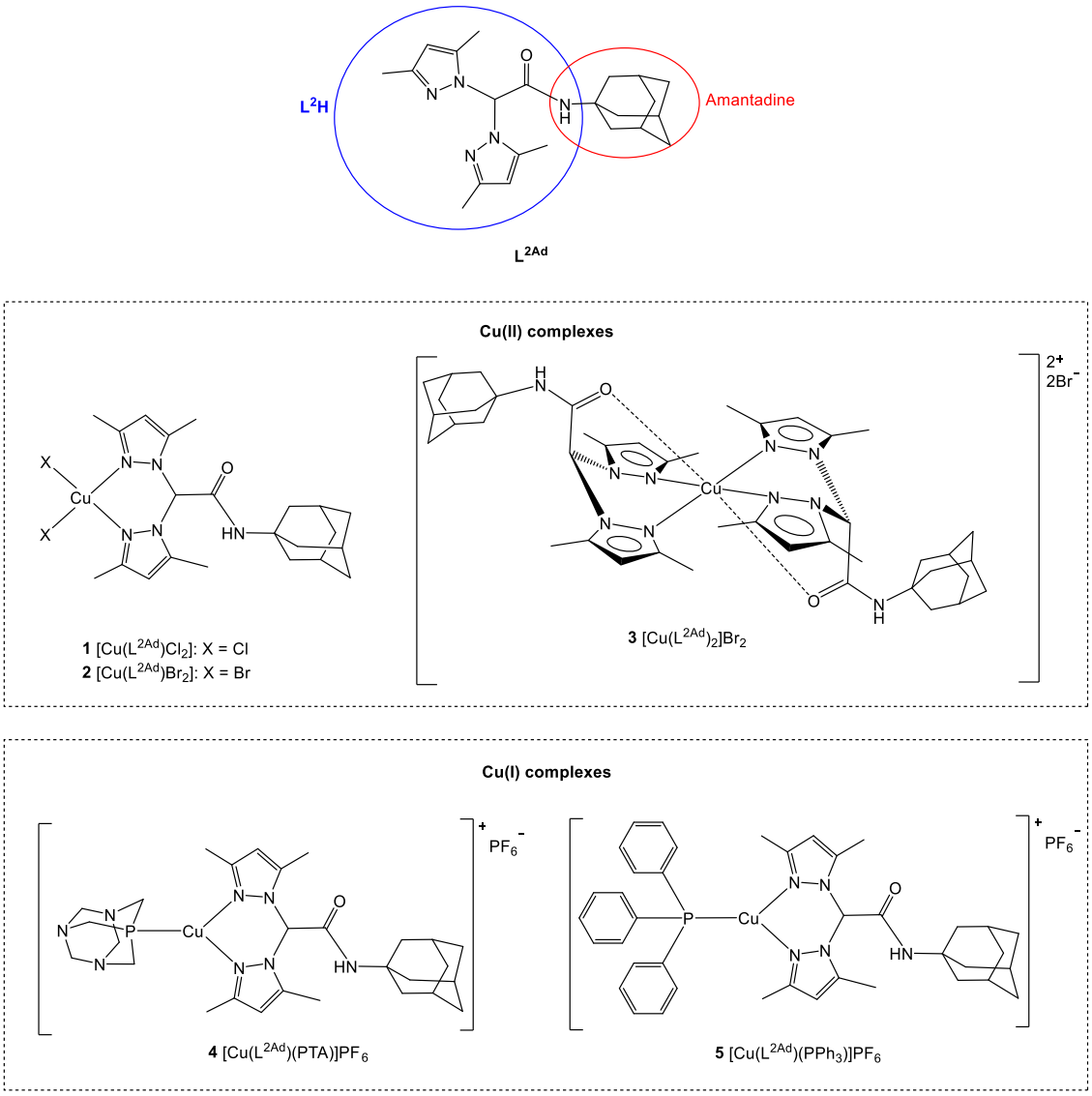

Figure 1. Structures of ligand L^{2Ad} and related complexes **1**−**5**.

to exert antiproliferative effects in glioma cell lines, through different mechanisms of action.[13−15] For example, the ionophore elesclomol is able to transport copper inside the mitochondria in glioblastoma (GBM) cells, where it induces the generation of ROS and cell death. Accordingly, the copper chelator ammonium tetrathiomolybdate (TTM) almost completely prevents this effect by depletion of bioavailable copper.[16] A fascinating study described the relationship between copper and temozolomide (TMZ), the standard postsurgical treatment of GBM,[17] in aqueous solution, demonstrating that copper coordinates the active and unstable TMZ metabolite 5-(3-methyltriazen-1-yl)imidazole-4-carboxamide (MTIC), enhancing its stability. Accordingly, copper-bound apoferritin was able to immobilize MTIC inside the protein scaffold, shielding it from decomposition. This system enhanced TMZ toxicity against GBM cells as the MTIC-copper complex could be dissociated by GSH, which is present at a high level in cytosolic tumor cells, and free MTIC could exert its DNA-alkylating activity.[18] It may be relevant to discuss these findings because, even if a better understanding of molecular mechanisms, biomarkers, and molecular pathogenesis of GBM has been gained, survival rates continue to be low.[19] A major obstacle to treatment failure lies in the aggressive behavior and the high degree of intratumor heterogeneity of this type of primary brain tumor.[20]

Our studies on anticancer Cu(I) and Cu(II) complexes by using several classes of ligands endowed with different lipophilicity helped to demonstrate that proper coordination improves the bioavailability and the cellular uptake of the complexes, and new modes of action can be obtained.[21−27] Recently, we have reported Cu(I) and Cu(II) complexes with significant cytotoxic effects against different human tumor cell lines obtained from ligands prepared by conjugating the terminal COOH group of the bifunctional species bis(pyrazol-1-yl)acetic acid (LH) and bis(3,5-dimethyl-pyrazol-1-yl)acetic acid (L^2H) to the primary NH_2 group of bioactive molecules interacting with specific targets.[28−31]

In the present study, the bifunctional species L^2H has been conjugated to the known drug amantadine to obtain the new ligand L^{2Ad}, which has been used as a chelator for the synthesis of the new Cu complexes **1**−**5** (Figure 1) to be evaluated as potential agents for the treatment of glioblastoma. Amantadine was selected as a bioactive molecule since it has recently been demonstrated to show from moderate to good antiproliferative

https://doi.org/10.1021/acs.jmedchem.4c00821
J. Med. Chem. XXXX, XXX, XXX−XXX

Scheme 1. Synthesis of Ligand L^{2Ad} and Complexes 1−5[a]

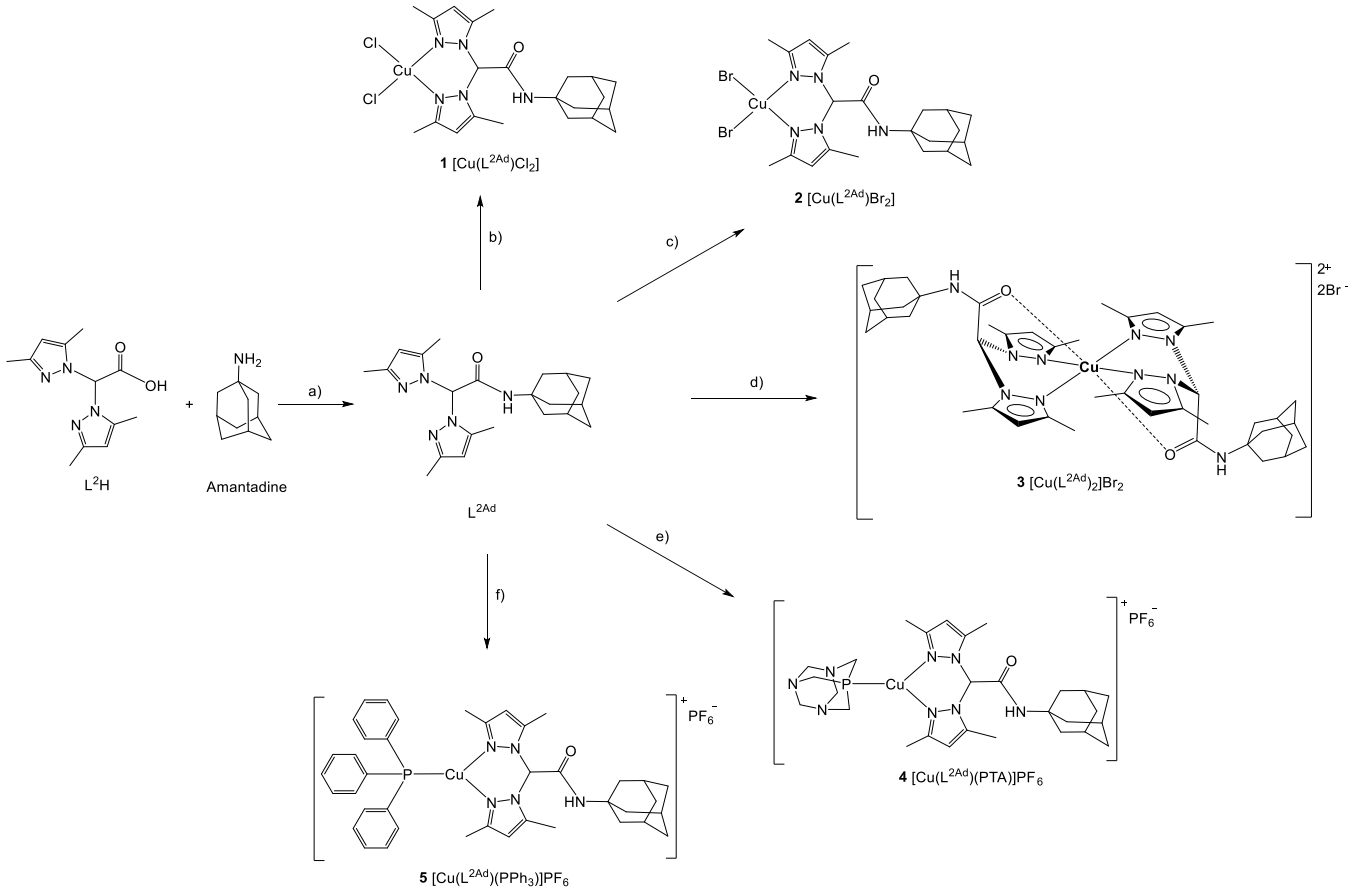

[a]Reagents and Conditions: (a) TBTU, DIPEA, DMF, rt 20 h; (b) 1 equiv $CuCl_2 \cdot 2H_2O$, CH_3CN, rt 24 h; (c) 1 equiv $CuBr_2$, CH_3CN, rt 20 h, then reflux 4 h; (d) 0.5 equiv $CuBr_2$, CH_3CN, reflux 24 h; (e) PTA, $Cu(CH_3CN)_4PF_6$, CH_3CN, rt 20 h, then reflux 3 h; (f) PPh_3, $Cu(CH_3CN)_4PF_6$, CH_3CN, rt, 24 h.

effects in different human tumor cell lines, including hepatocarcinoma, melanoma, and glioblastoma cells.[32−34] Moreover, Pt-based complexes functionalized with amantadine have already been reported to display promising cytotoxic activity against various human tumor cell lines.[35] Finally, amantadine consists of a primary amine group suitable to be conjugated to the carboxylic group of the bifunctionalizable species L^2H and the bioversatile adamantyl scaffold, which characterizes several derivatives identified as anticancer agents.[35,36]

L^{2Ad} has served for the preparation of three Cu(II) complexes (**1**−**3**) and two Cu(I) complexes (**4** and **5**). In the latter case, the hydrophilic 1,3,5-triaza-7-phosphaadamantane (PTA) and the lipophilic triphenylphosphine (PPh_3) were used as coligands to stabilize Cu in the +1 oxidation state, conferring different solubility properties to the corresponding complexes (Figure 1).

The molecular structures of the new complexes were investigated by means of X-ray photoelectron spectroscopy (XPS) and X-ray absorption spectroscopy (NEXAFS, XAS). In addition, single-crystal X-ray diffraction analyses were performed to determine the molecular structure of the cationic complex **3**.

Finally, the new complexes **1**−**5** and the corresponding uncoordinated ligand L^{2Ad} were investigated for their antitumor potential on three different GBM cell lines (U87, T98, U251) and for their ability to enhance the chemosensitivity to TMZ.

2. RESULTS AND DISCUSSION

2.1. Synthesis and Characterization. *2.1.1. Synthesis of Ligand L^{2Ad}.* Ligand L^{2Ad} was prepared following the one-step synthesis reported in Scheme 1. Amantadine was reacted with L^2H in the presence of 2-(1H-benzotriazole-1-yl)-1,1,3,3-tetramethylaminium tetrafluoroborate (TBTU) and diisopropylethylamine (DIPEA) at room temperature for 20 h. After separation and purification by column chromatography, L^{2Ad} was obtained in a reasonable yield (86%, Mp. 132−133 °C). The IR spectrum carried out on a solid sample of L^{2Ad} showed all of the expected bands for the ligand. Specifically, weak absorptions due to the CH stretching have been observed in the range 2848−3080 cm^{-1}, while a peak due to the amide stretching (N−H) is present at 3300−3324 cm^{-1}. The stretching of the C═O group is detected as a strong peak at 1671 cm^{-1}, in the typical range for the amide groups. The (C═C/C═N) peaks are detected as medium-intensity peaks at 1554 cm^{-1}. The ^1H NMR and ^{13}C NMR spectra of L^{2Ad} in $CDCl_3$ solution showed all the expected signals for the ligand, and the two-dimensional (2D) Heteronuclear Single Quantum Coherence (HSQC) experiment, used to determine proton-carbon single bond correlations, allowed the complete assignment of all ^1H and ^{13}C NMR signals. A single set of resonances appears for the pyrazole rings, indicating that they

https://doi.org/10.1021/acs.jmedchem.4c00821
J. Med. Chem. XXXX, XXX, XXX−XXX

are equivalent. The ESI-MS study was performed by dissolving the ligand in CH_3CN and recording the spectra in positive- and negative-ion modes. The molecular structure of L^{2Ad} is confirmed by the presence in the positive-ions spectrum of the molecular peaks at m/z 382, 404, and 420, due to the $[L^{2Ad} + H]^+$, $[L^{2Ad} + Na]^+$ and $[L^{2Ad} + K]^+$ species, respectively. The elemental analysis gives a positive matching between the calculated and the measured values for C, H, and N.

2.1.2. Synthesis of Cu(II) Complexes 1−3. The copper(II) complexes $[Cu(L^{2Ad})Cl_2]$ (**1**) and $[Cu(L^{2Ad})Br_2]$ (**2**) were synthesized using the acceptors $CuCl_2·2H_2O$ and $CuBr_2$, respectively, with the ligand L^{2Ad} in the stoichiometric ratio 1:1 in CH_3CN (Scheme 1). The reaction was performed at room temperature (rt) for the synthesis of $[Cu(L^{2Ad})Cl_2]$ and at reflux for the synthesis of $[Cu(L^{2Ad})Br_2]$. Complex $[Cu(L^{2Ad})_2]Br_2$ (**3**) was obtained by using L^{2Ad} and $CuBr_2$ in the stoichiometric ratio 2:1 in CH_3CN (Scheme 1). Bromide is less coordinative than chloride, allowing the coordination of copper with two ligands. The corresponding complex with chlorine $[Cu(L^{2Ad})_2]Cl_2$ was not obtained by using $CuCl_2·2H_2O$ as an acceptor and performing the reaction in a 2:1 stoichiometric ratio. FT-IR spectra show all of the expected bands for the complexes; in particular, it is possible to observe strong absorptions due to the asymmetric stretching of the C═O group in the range 1634−1664 cm^{-1}, with slight variation with respect to the stretching of the same group (1671 cm^{-1}) for the ligand L^{2Ad}. In the far-infrared spectrum of **1**, a very strong absorption at 280 cm^{-1} due to the stretching frequencies of the Cu−Cl bond can be observed. Likewise, strong absorptions due to the Cu−Br stretching frequencies are detected in the range 232−281 cm^{-1} in the far-infrared spectra of **2** and **3**.[37] The ESI-MS spectra of the complexes **1**−**3** were performed dissolving **1** and **2** in CH_3OH and **3** in CH_3CN. Concerning ESI-MS(+) of complex **1**, peaks at m/z 135 and 413 are due to the species $[CuCl_2 + H]^+$ and $[Cu(L^{2Ad})_2]^{2+}$, respectively. The ESI-MS(+) spectra of complexes **2** and **3** show peaks at m/z 413 and 525, due to the fragments $[Cu(L^{2Ad})_2]^{2+}$ and $[Cu(L^{2Ad})Br]^+$. For complex **3** the additional signal at m/z 906, due to the fragment $[Cu(L^{2Ad})_2Br]^+$, further confirms the presence of two ligands that coordinate copper.

2.1.3. Synthesis of the Cu(I) Complexes 4 and 5. The copper(I) complexes $[Cu(L^{2Ad})(PTA)]PF_6$ (**4**) and $[Cu(L^{2Ad})(PPh_3)]PF_6$ (**5**) were synthesized in CH_3CN using, as starting materials, the ligand L^{2Ad}, the metallic acceptor $[Cu(CH_3CN)_4]PF_6$ and the phosphane coligands PTA or PPh_3 for **4** or **5**, respectively. Spectroscopic analyses such as FT-IR, ^1H NMR, $^{31}P\{^1H\}$-NMR, and ESI-MS confirm the stoichiometry of the synthesized complexes. All of the expected absorption bands were observed in the FT-IR spectra. In particular, in the range 2857−3152 cm^{-1}, the complexes exhibit weak bands typical of C−H stretching. The strong absorptions at 1671 and 1672 cm^{-1} for **4** and **5**, respectively, represent the asymmetric stretching of the carbonyl groups. Moreover, bands in the range 1417−1561 cm^{-1} are due to the C═C/C═N stretching vibrations. Finally, very intense absorption bands are visible at 834 and 835 cm^{-1} in the spectra of **4** and **5**, respectively, indicating the stretching of the PF_6^- counterion. The ^1H NMR spectra, performed in CD_3CN and $CDCl_3$ for **4** and **5**, respectively, confirm the stoichiometric ratio between heteroscorpionate ligand and phosphane coligands. They showed a single set of resonances for the pyrazole rings, indicating that the pyrazole protons are equivalents, with a slight shift due to the coordination of the metal center. Moreover, the signals of adamantanamine are clearly visible at δ 1.58−2.55 ppm. The signals at δ 6.58 and 6.81 ppm point to the α−C*H* proton, while the 4−C*H* hydrogens of the pyrazoles are detectable at δ 6.03 and 5.39 ppm for **4** and **5**, respectively. The shift observed for the pyrazole rings is the result of coordination with the metal copper acceptor. The CH_2 protons of PTA coligand of **4** are visible at δ 4.13−4.62 ppm, while the aromatic hydrogens of PPh_3 coligand of **5** are found at δ 7.41−7.60 ppm. The ^{31}P NMR spectrum of complexes **4** and **5**, performed in CD_3CN and $CDCl_3$, gives broad singlet peaks at −94.35 and 7.49 ppm, respectively, downfield shifted with respect to the value of the free phosphanes in the same solvent (δ −102.07 ppm for PTA in CD_3CN and δ = −5.36 ppm for PPh_3 in $CDCl_3$). Moreover, the spectra show distinctive septets due to the presence of the PF_6^- counterion at −144.62 and −144.02 ppm, respectively. The ESI-MS study was performed by dissolving complexes **4** and **5** in CH_3CN, recording the spectra in ion-positive and ion-negative modes. ESI-MS(+) spectrum of complex **4** showed a peak at m/z 485, which can be attributed to the $[Cu(L^{2Ad}) + CH_3CN]^+$ species. Moreover, a fragment at m/z 601, due to the $[Cu(L^{2Ad})(PTA)]^+$ species, confirms the presence and stability of the complex. ESI-MS(+) spectrum of complex **5** showed fragments at m/z 366 and 587, relative to the $[Cu(PPh_3) + CH_3CN]^+$ and $[Cu(PPh_3)_2]^+$ species, respectively. Both peaks show the coordinative bond between copper and phosphines. Moreover, the fragment at m/z 706, due to the $[Cu(L^{2Ad})(PPh_3)]^+$ species, confirms the presence of the complex. In the negative-ion spectra of **4** and **5**, $[PF_6]^-$ was observed as the major peak at m/z 145.

2.1.4. Stability Analysis for Complexes 1−5 in DMSO Solution. Complexes **1**−**5** were analyzed by UV−vis spectroscopy at 240−900 nm (Figure S1). UV−vis spectra of complexes **1**−**5** were also recorded to observe their stability in DMSO. The purpose of this investigation was to evaluate the changes in the absorbance values for the single complexes in order to determine the possibility of performing the cytotoxicity tests. The analysis was conducted by dissolving 2 mmol of each compound in 25 mL of DMSO. The analysis was performed at time 0, after 24, 48, and 72 h in the range of 240−740 nm. The collected spectra for all the complexes are reported in the Supporting Information (Figure S2), and their analysis showed that all compounds are highly stable in DMSO solution up to 72 h. Preliminary stability studies of the more active complexes **3** and **5** were also performed in the presence of GSH (1:1 in DMSO and 1:10 in DMSO/H_2O 80:20, due to the low solubility of GSH in DMSO) after 2, 5, 7, and 10 min. The results reported in the Supporting Information (Figure S3) highlighted that both complexes are GSH-labile at a 1:10 ratio. Cu(II) complex **3** is also unstable in the presence of GSH at a 1:1 ratio, probably due to both reduction of Cu(II) to Cu(I) and coordination.[18,38,39]

2.2. X-ray Diffraction Studies. *2.2.1. Crystal Structure of Complex 3.* A summary of crystallographic data collection and refinement parameters for complex **3** is shown in Table 1, while Table 2 lists some selected bond lengths and angles (full listings of metrical data are given in Tables S1 and S2). The crystal structure belongs to the *I2/m* monoclinic space group; each $[Cu(L^{2Ad})_2)]^{2+}$ unit cocrystallizes with two acetonitrile, four water molecules, and two disordered bromide anions. Two L^{2Ad} molecules coordinate the central Cu(II) atom in a

https://doi.org/10.1021/acs.jmedchem.4c00821
J. Med. Chem. XXXX, XXX, XXX−XXX

Table 1. Summary of Data Collection Parameters and Crystal Data for Complex 3[a]

radiation	Cu Kα (λ = 1.54184)
empirical formula	$C_{48}H_{72}Br_2CuN_{12}O_6$
formula weight	1136.53
temperature/K	301(1)
crystal system	monoclinic
space group	*I*2/*m*
a/Å	14.43090(10)
b/Å	11.39650(10)
c/Å	16.88770(10)
α/°	90
β/°	93.8660(10)
γ/°	90
volume/Å^3	2771.06(4)
Z	2
ρ_{calc} g/cm^3	1.362
μ/mm^{-1}	2.694
F (000)	1182.0
crystal size/mm^3	0.54 × 0.5 × 0.34
reflections collected	45302
independent reflections/R_{int}	2896/0.0313
restraints/parameters	19/199
goodness-of-fit on F^2	0.929
final R (R_1; wR_2) indexes [$I > 2\sigma$ (I)]	0.0602, 0.1859
largest diff. peak/hole/e Å^{-3}	1.15/−0.48

[a]Goodness−of−fit = $[\Sigma\ (w\ (F_0^2 - F_c^2)^2]/(N_{obsvns} - N_{params})]^{1/2}$, based on all data; $R_1 = \Sigma\ ||F_0| - |F_c||/\ \Sigma\ |F_0|$; $wR_2 = [\Sigma\ w\ (F_0^2 - F_c^2)^2/\ \Sigma\ w\ (F_0^2)^2]^{1/2}$.

trans-facial manner through the carbonyl O1 oxygen and the N2 nitrogen atoms of two pyrazole rings (Figure 2a).

Notably, the bis(3,5-dimethyl-1H-pyrazol-1-yl)acetyl-adamantan-1-amido ligand has been reported only in a dinuclear aluminum complex so far,[40] hence, to the best of our knowledge, this is the first example of a copper(II) complex containing this moiety. The pyrazole N2 nitrogen atoms of two L^{2Ad} ligands take four coordinating equatorial positions; the two carbonyl O1 oxygens coordinate axially with the metal on opposite sides of this plane, defining an overall distorted octahedral geometry. The main deviation from ideality, besides the expected difference in bond lengths between copper and the nitrogen and oxygen atoms underlining a tetragonal elongation of the octahedron (Cu−N 2.0200(19) Å, Cu−O 2.346(2) Å), is due to the strain imposed by chelation, which prevents the O1−Cu−O1^2 (O1^2 at 1 − *x*,1 − *y*,2 − *z*) axis to be perfectly orthogonal to the equatorial plane (angle of 82.9°). Upon coordination, each L^{2Ad} molecule forms three six-membered cyclometallate rings. All of them show a common *boat* conformation with the same atoms, C2 and Cu1, occupying the "stern" and "prow" positions. The copper atom takes a special position in the unit cell, lying on a 2-fold proper rotation axis and on a mirror plane (Figure 2c,d). Due to symmetry, the atoms of the pyrazolyl rings and those belonging to the acetylamido group linking the adamantane moiety are exactly coplanar, so that the mean planes encompassing the rings and the linker are perfectly staggered and make with each other angles of 60°. Similarly, the planes passing through the acetylamido linker and each pyrazolyl ring makes with equatorial plane angles of 90 and 44.5°, respectively. A search in the CCDC repository[41,42] showed some Cu(II) complexes of bis-pyrazolyl acetate,[43−50] among which few bis-pyrazolyl acetamide derivatives;[45] other bis-pyrazolyl acetamide ligands, including the one present in the above-named aluminum complex[40] are also known.[51−59] With one exception,[49] reported bis-pyrazolyl acetate copper derivatives share a *trans-fac* coordination of the tridentate ligand with mean values of the O−Cu−O and O−Cu−N angles of 179.7 and 94.8°, similar to those found in this work. Likewise, the mean values of the Cu−N and Cu−O bonds are 2.055 and 2.276 Å; in **3** these bonds are 0.035 and 0.070 Å shorter than such means, respectively, but within the known ranges (1.972−2.438 Å for Cu−N and 1.936−2.540 Å for Cu−O). Distances within pyrazolyl rings agree with those of known complexes,[43−50] as well as those of similar compounds recently investigated by our group.[60] The C1−O1 bond (1.231(4) Å) and the C1−C2 bond (1.549(4) Å) have in turn elongated double-bond and single-bond character, giving no evidence of conjugation outside the pyrazolyl rings. The C1−N1 and N1−C8 distances (1.316(4) and 1.481(4) Å, respectively), typical of an amide linkage, agree well with the mean values found for pyrazolyl acetamide ligands[51−59] (1.330, 1.457 Å) and even better if considering the same values specifically pertaining to acetamide ligands involved in coordination (1.322, 1.463 Å).[45,52,55,59]

Notably, the amide nitrogen N1 establishes a hydrogen bond with the O3 oxygen of a water molecule (*w*1) (Figure 2b). At an average distance of 2.15 Å from *w*1, an undefined ring of electron density is positioned on a 2-fold proper rotation axis and a mirror plane. The disorder, placed across symmetry

Table 2. Selected Bond Lengths (Å) and Angles (°) for Complex 3

bond		angle		angle	
Cu1−N2	2.0200(19)	O1−Cu1−O1[a]	180.00(7)	C2−N3−N2	119.89(19)
Cu1−O1	2.346(2)	N2[b]−Cu1−N2[c]	180.00(9)	C1−C2−N3	110.45(16)
N2−N3	1.372(3)	N2−Cu1−N2[b]	86.44(11)	O1−C1−C2	119.5(3)
N2−C3	1.333(3)	N2−Cu1−N2[c]	93.56(11)	N1−C1−O1	126.1(3)
N3−C5	1.354(3)	N2−Cu1−O1	85.22(7)	N2−C3−C4	110.0(2)
N3−C2	1.454(3)	O1−Cu1−N2[c]	94.78(7)	N3−C5−C4	106.2(2)
C3−C4	1.400(4)	Cu1−O1−C1	115.0(2)	C3−C4−C5	106.9(2)
C4−C5	1.363(4)	Cu1−N2−N3	117.81(14)	C1−N1−C8	127.0(3)
C1−O1	1.231(4)	C3−N2−N3	105.25(19)	N1−C1−C2	114.4(3)
C1−C2	1.549(4)				
N1−C1	1.316(4)				
N1−C8	1.481(4)				

[a]1 − *x*,1 − *y*,2 − *z*. [b]+*x*,1 − *y*,+*z*. [c]1 − *x*,+*y*,2 − *z*.

https://doi.org/10.1021/acs.jmedchem.4c00821
J. Med. Chem. XXXX, XXX, XXX−XXX

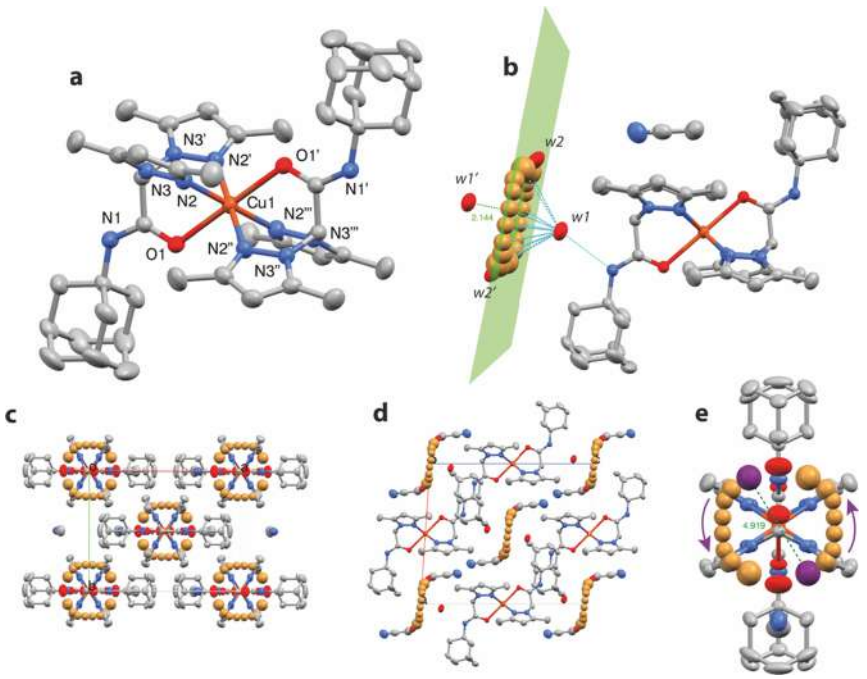

Figure 2. (a) $[Cu(L^{2Ad})_2]^{2+}$ complex cation. Hydrogen atoms are omitted for clarity, and ellipsoids are drawn at 50% probability. For simplicity, the symmetry-equivalent positions of the N and the O atoms are indicated with primed labels. (b) Hydrogen bond interactions (cyan dashed lines) between N1, *w*1, *w*2, *w*2' and the disordered bromide anions. *w*1' distance to the bromide ring plane (in green) is highlighted with a dashed green line. A solvated acetonitrile molecule (not involved in hydrogen bonding) is also visible. (c) Crystal packing shown along the *c* axis. (d) Crystal packing shown along the *b* axis. (e) Bromide anions pair (highlighted in purple) maintains a constant distance of approximately 5 Å (dashed green line) but is free to rotate between *w*2 and *w*2' in the crystal. All figures have been prepared using the *Mercury* program.[61]

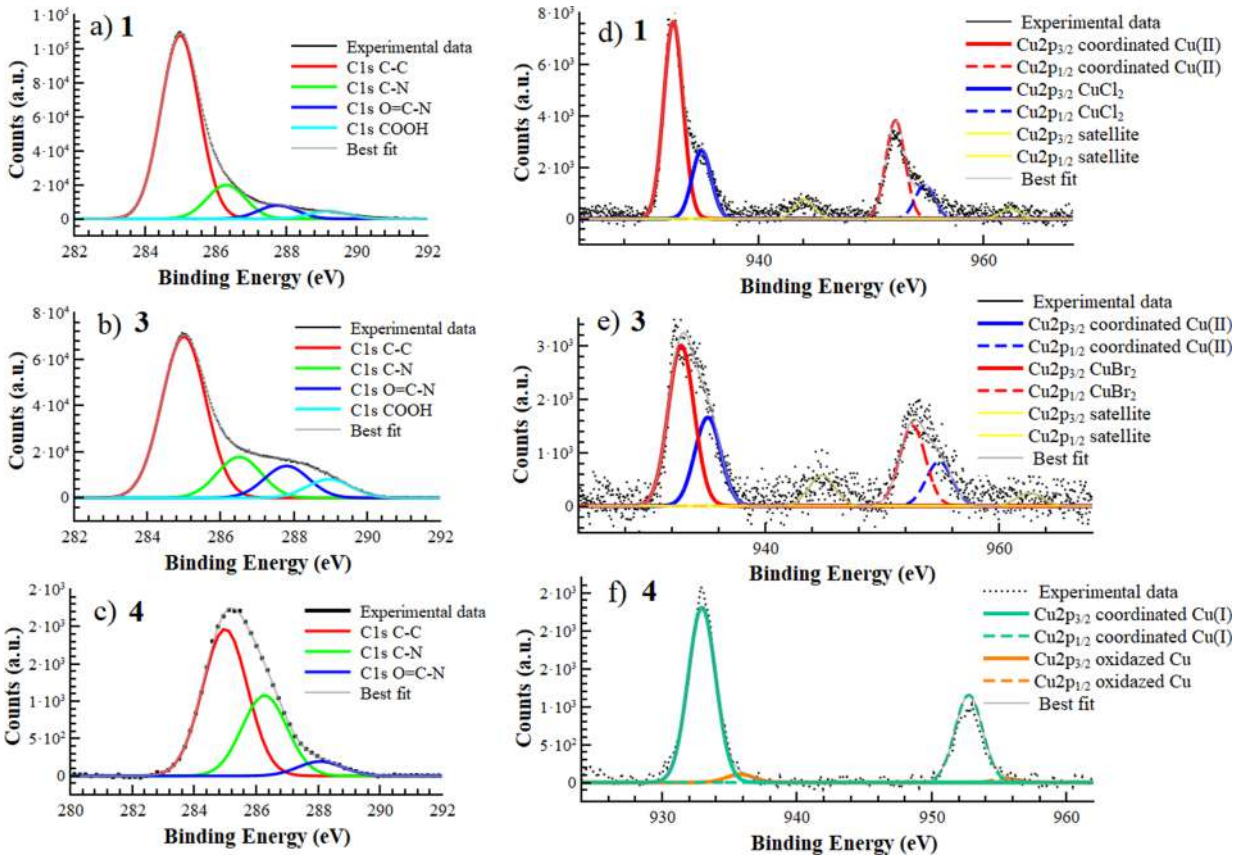

Figure 3. XPS spectra collected on Cu(II) and Cu(I) complexes at C 1s (a−c) and Cu 2p (d−f) core levels. Spectra collected on complex **1** are representative for both **1** and **2**; similarly, spectra collected on complex **4** are representative for both complexes **4** and **5**.

https://doi.org/10.1021/acs.jmedchem.4c00821
J. Med. Chem. XXXX, XXX, XXX−XXX

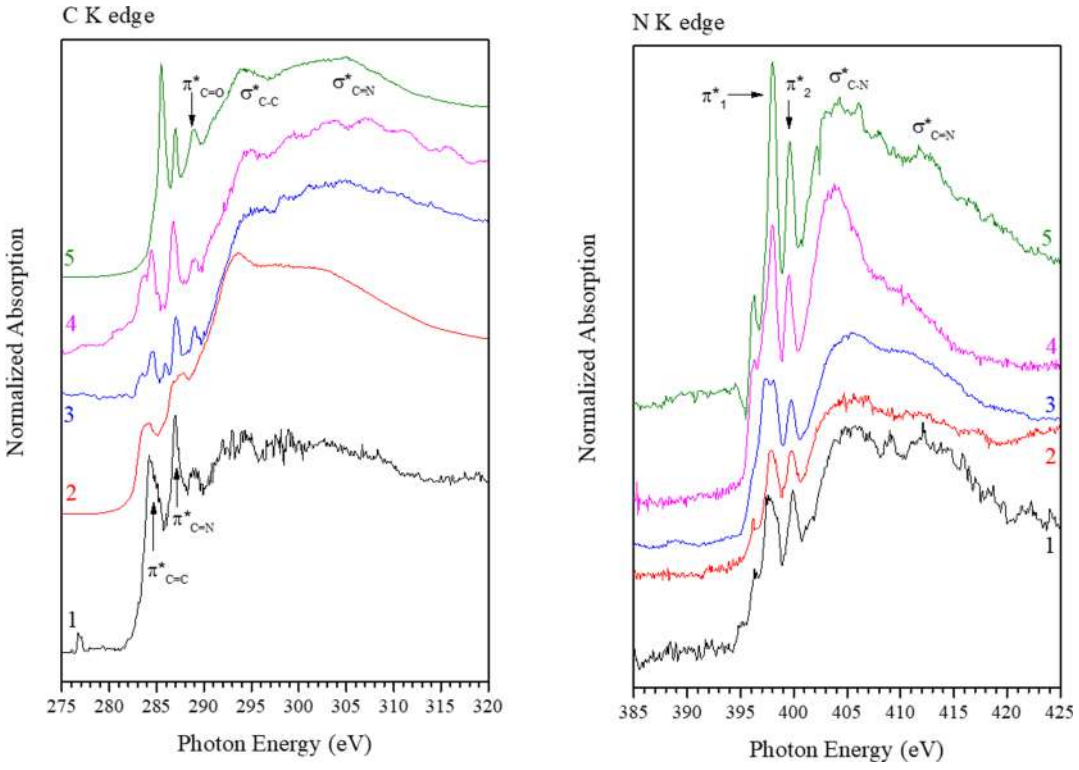

Figure 4. C K edge (left) and N K edge (right) NEXAFS spectra of samples **1**−**5**; the complex number is indicated in the picture near each spectrum.

elements, made the modeling of this region particularly challenging. By evaluating the crystal packing, a second water molecule (related to the first by symmetry, *w*1') is placed at the same distance from the ring, which is sandwiched between the two water molecules. Numerous attempts to model this unclear electron density have been made. As two bromide anions outside of the copper coordination sphere are expected, the model we built was that in which two additional water molecules, *w*2 and *w*2', opposite to each other and lying outside the ring plane, divide the ring into two parts, each of them containing one disordered bromide anion. The two anions probably face each other maintaining a reciprocal distance of about 5 Å to minimize charge repulsion (Figure 2e). Their disordered position over the crystal lattice results in the smear of electron density (Figure S4a,b), which was therefore modeled (using an isotropic description in the asymmetric unit) with four different positions and a summed occupancy of 0.5, considering symmetry restraints. Attempts to introduce hydrogen atoms riding on water molecules *w*2 and *w*2' led always to nonconvergent models during refinement, so they were omitted. As seen above, however, the overall challenge posed by the disordered position of the bromide anions did not affect the description of the structurally well-characterized $[Cu(L^{2Ad})_2]^{2+}$ complex cation. Quite expectedly, the cocrystallized water molecules and the disordered bromide ions are involved in most of the nonbonding interactions; a detailed description of these contacts is provided in the Supporting Information together with an extended version of the structural commentary (see Figures S5−S7 and Table S3).

2.3. SR-XPS and NEXAFS Investigation of the Molecular and Electronic Structure. *2.3.1. SR-XPS Analysis of Cu(II) Coordination Compounds.* Synchrotron radiation-induced X-ray photoelectron spectroscopy (SR-XPS) measurements allowed the interaction between Cu(II) and the L^{2Ad} ligand to be probed in the three Cu(II) complexes $[Cu(L^{2Ad})Cl_2]$ (**1**), $[Cu(L^{2Ad})Br_2]$ (**2**) and $[Cu(L^{2Ad})_2Br_2]$ (**3**). Spectra were collected at C 1s, N 1s, O 1s, Br 3d, Cl 2p and Cu 2p core levels. Complete SR-XPS data analysis results (binding energy − BE (eV), full-width half maximum−fwhm (eV), atomic percentages, and proposed assignments for all measured signals components) are reported in the Supporting Information (Table S4). C 1s spectra (Figure 3a,b) are composite; by applying a peak-fitting procedure, it is possible to individuate at least four components associated with C−C aliphatic carbons (285.0 eV BE), C−N (286.3 eV BE), N−C═O bond (287.7 eV BE) and COOH groups (289.0 eV BE), confirming the stability of L^{2Ad}. N 1s spectra of **1** and **3** show three components at about 399.6, 401.2, and 402.5 eV BE, respectively, associated with N−N and N═N, N−C═O, and N^+. In Complex **2** only the first two contributions are observed. Cu 2p spectra (Figure 3d, e) have two components at about 932.5 and 935.0 eV BE, respectively associated with Cu(II) in the coordination complex[62,63] and $CuCl_2$ or $CuBr_2$.[64]

Finally, the Cl 2p spectrum of **1** is composite, showing two spin-orbit pairs indicative of Cl−Cu of the coordination complex at lower binding energy, and $CuCl_2$, at higher binding energy.[63,65] Br 3d spectra of **2** and **3** are both composite by two spin-orbit pairs whose Br $3d_{5/2}$ component is located around 68.6 and 71.3 eV BE, indicative for Br−Cu in the coordination complex and $CuBr_2$, respectively.[63]

2.3.2. SR-XPS Analysis of Cu(I) Coordination Compounds. Similarly to Cu(II) complexes, SR-XPS spectra of the two Cu(I) coordination compounds **4** and **5** were collected at C 1s, N 1s, F 1s, O 1s, P 2p, and Cu 2p core levels (all Binding Energy, BE (eV), fwhm (eV), atomic percentages, and proposed signals assignments are reported in the Supporting

https://doi.org/10.1021/acs.jmedchem.4c00821
J. Med. Chem. XXXX, XXX, XXX−XXX

Information, Table S5). C 1s spectra of **4** and **5** (Figure 3c) show three components at about 285.0, 286.3, and 288.0 eV BE, respectively associated with C−C, C−N, and N−C=O as expected for the structure of L^{2Ad}. For both samples, F 1s spectra show a single component located at about 686.5 eV BE confirming the presence of PF_6^-. N 1s spectra have two components located at 399.4 and 401.2 eV BE for sample **4**, and at 400.1 and 401.4 for **5**, respectively, associated with N−N and N=N, N−C=O (not distinguishable within the selected resolution). P 2p spectra show two components: for sample **4**, P $2p_{3/2}$ spin−orbit components are observed at 130.9 and 136.3 eV BE, as expected for PTA and PF_6^-; for **5**, P $2p_{3/2}$ BEs are positioned at 131.4 and 136.6 eV, coherently with PPh_3 and PF_6^-. As for Cu 2p spectra (Figure 3f), both samples have two pairs of spin−orbit components arising by a main signal at about 933.0 and a smaller contribution at 935.0 eV, suggesting the presence of a large amount of Cu(I)[64] (about 95%, see Table S4) and a nearly 5% of Cu(II) ions, probably arising by the spontaneous oxidation of copper(I) ions during the deposition procedure or under the SR X-ray beam.

2.4. NEXAFS Spectroscopy. The molecular and electronic structure of complexes **1**−**5** was investigated also by Near Edge X-ray Absorption Fine structure (NEXAFS) spectroscopy at the C K and N K edges; experiments were carried out on thin films of the investigated complex and the recorded spectra are shown in Figure 4. A summary of the peak positions and assignments is given in Table 3. The spectra of the five

Table 3. Peak Position (eV) and Relative Assignment of the Main Features Appearing in the C and N K Edge NEXAFS Spectra of Samples 1−5

sample	1	2	3	4	5	assignment
C K edge	284.2	284.3	284.2	284.3	284.3	$\pi^*_{C=C}$
	286.9	287.3	286.9	286.8	286.9	$\pi^*_{C=N}$
	288.9		288.9	288.9	288.8	$\pi^*_{C=O}$
	293.8	293.7	294.6	294.5	294.0	σ^*_{C-C}
	303.0	303.0	303.0	303.0	303.0	$\sigma^*_{C=N}$
N K edge	397.8	397.9	397.9	398.0	398.0	π^*_1
	399.8	399.8	399.7	399.6	399.6	π^*_2
	405.6	405.6	405.3	403.8	404.2	σ^*_{C-N}
	412	412	411	411	412	$\sigma^*_{C=N}$

complexes are very similar to each other and therefore they will be discussed together. In the C K edge spectra (left-hand side picture) of sample **1** the two prominent peaks below the edge are assigned to C 1s → π^* transitions related to C=C ($\pi^*_{C=C}$, 284.2 eV) and C=N ($\pi^*_{C=N}$, 286.9 eV) transitions related to the pyrazole rings in the L^{2Ad} ligand, as already reported.[28,66] A third C 1s → π^* transition at 289.0 eV ($\pi^*_{C=O}$) is related to the C=O bonds of the amide functions of the L^{2Ad} ligand. Above the edge two broad s* resonances are mainly due to C−C (σ^*_{C-C}, 293.8 eV) and C=N ($\sigma^*_{C=N}$, 303 eV).[67] In the spectrum of sample **2** the $\pi^*_{C=C}$ and $\pi^*_{C=N}$ resonances appear broadened, probably due to the quality of the thin film, and the $\pi^*_{C=O}$ resonance is not visible, being covered by the edge jump and the broad σ^*_{C-C} resonance. The spectra of samples **3** and **4** resemble sample **1**, with a spurious peak at about 283.7 eV, probably due to carbon contamination of the beamline optics. In the spectrum of sample **5**, the $\pi^*_{C=C}$ resonance appears to be more intense with respect to the spectra of the other samples, being mainly due to C 1s → π^* transitions of the C=C bonds of the triphenylphosphine ligand. In the N K edge spectra (right-hand side picture) of all the five samples, the two peaks detected below the edge, labeled π^*_1 and π^*_2 in Figure 4 and Table 3, are assigned to N 1s → π^* transitions arising from nitrogen atoms of the pyrazole rings.[28,66] Above the edge, two broad σ^* resonances arising from the C−N (σ^*_{C-N}) and C=N ($\sigma^*_{C=N}$) bonds are detected.

2.5. Local Geometry around Cu Ions: XAFS Studies. The Cu K edge X-ray absorption fine structure spectroscopy (XFAS) technique was applied to determine the average valence state, coordination chemistry, and local atomic structure around the Cu sites. The XAFS data were analyzed in the near edge (XANES) and extended (EXAFS) regions, that provide complementary information. The XANES features provide valuable information about the valence state and coordination symmetry of the absorber, in a complementary way the analysis of the EXAFS features describes the local atomic structure around the absorber in terms of neighbor coordination shells.[68] To obtain reliable quantitative information from the EXAFS data analysis, it is important to have approximate structural models (atomic clusters) of the structure around the absorber, from which the amplitude and phase functions, required to calculate the theoretical EXAFS functions, can be determined. For complex **3** we used as an atomic cluster model the crystallographic structure; for complexes **1**, **2**, **4**, and **5**, we calculated realistic atomic clusters using the density functional theory (DFT), following a well-established scheme from other similar studies.[69]

2.5.1. Structural Models for XAS Data Analysis: Density Functional Theory (DFT) Calculations. The atomic cluster models around Cu sites in complexes **1**, **2**, **4**, and **5** were determined by DFT starting with a reasonable guess geometry, generated using the 3D open-source software Avogadro.[70] DFT calculations were achieved using the open-source software ORCA 5.0.1 (using Becke '88 exchange and Perdew '86 correlation integrals within the energy functional).[71,72] Karlsruhe orbital basis sets such as def2-SVP (Valence Double Zeta) and def2-TZVP (Valence Triple Zeta) were used, respectively, for lighter atoms and for Cu atoms. The Cu compound models were relaxed to an absolute minimum of energy using the Quasi-Newton method. The local Cu coordination clusters, obtained by XRD (complex **3**) or DFT (complexes **1**, **2**, **4**, and **5**) are presented in Figure 5. The atomic clusters were used to individuate the main scattering paths (single scattering, SS, or multiple scattering, MS) and calculate (using FEFF8 program[73]) the theoretical amplitude and scattering functions required to build the theoretical EXAFS functions.

2.5.2. XAS Data Analysis. The Cu K edge X-ray absorption spectroscopy (XAS) measurements were carried out at the European Synchrotron Radiation Facility (ESRF), on beamline BM08[74] (proposals ESRF ih-md58 and CERIC #20232011) on the Cu(I) (**4** and **5**) and Cu(II) (**1**−**3**) complexes with the aim to describe their local atomic structure around the absorber.

The normalized Cu XANES spectra for complexes **1**, **2**, and **3** (alongside that of metallic Cu, for the sake of reference) are shown in Figure 6a. The edge position/shape is compatible with the Cu(II) oxidation state in these complexes.[75] The chloride complex **1** shows a characteristic intense edge peak at 8984 eV associated with the 1*s* → 4*p* dipole-allowed transition. This peak disappears in complexes **2** and **3** that only depict

https://doi.org/10.1021/acs.jmedchem.4c00821
J. Med. Chem. XXXX, XXX, XXX−XXX

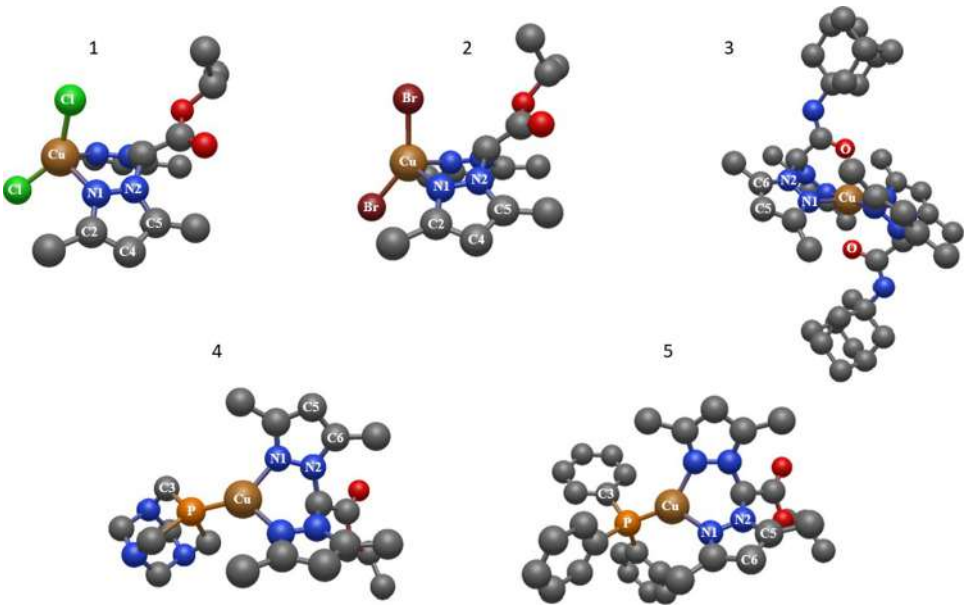

Figure 5. DFT-optimized models for Cu(II) (**1**, **2** and **3**) and Cu(I) (**4** and **5**) coordination compounds. The neighbors involved in the most intense scattering paths are highlighted in the image. Numbering of the different neighbors follows the increase in radial distance from the absorber, hence, in some cases across different samples, some scattering paths end up being named differently despite describing the same path (i.e., Cu−N1−C4 in complexes **1** and Cu−N1−C5 in complexes **3**, **4** and **5**).

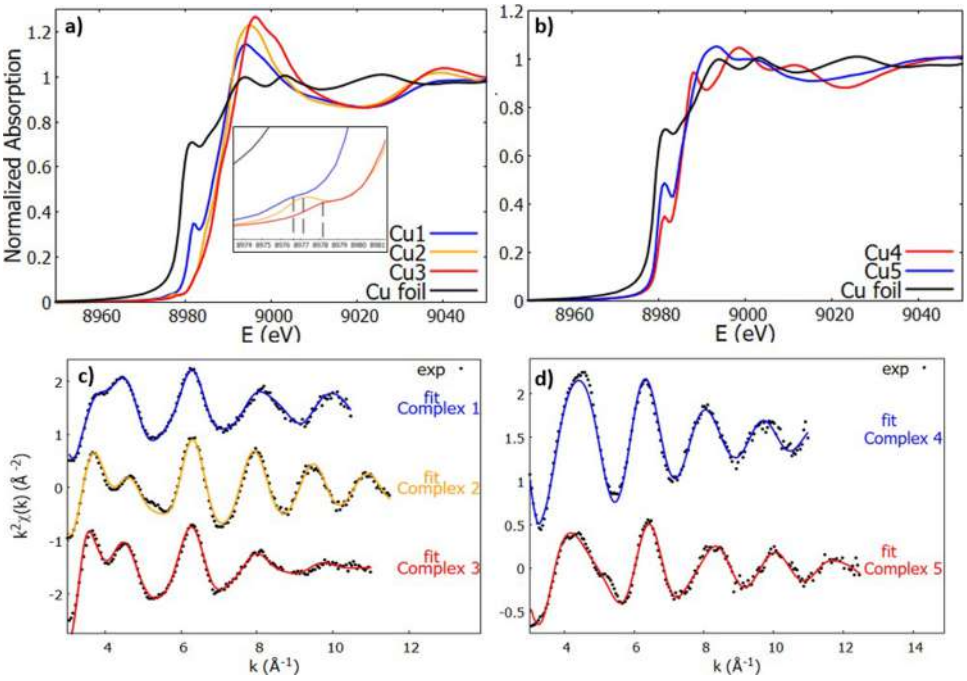

Figure 6. (a, b) Cu K edge and XANES region for Cu(II) and Cu(I) complexes (inset highlights the pre-edge region peaks). Comparison between experimental and obtained fit in K space for Cu(II) complexes (c) and Cu(I) (d).

tiny peaks (inset of Figure 6a), typical of Cu(II) sites, associated with dipole forbidden $1s \rightarrow 3d$ transitions. The disappearance of the $1s \rightarrow 4p$ peak in complexes **2** and **3** is likely related to a different geometric configuration. Complex **1** is arranged in a square planar geometry while complex **2** is in a tetrahedral geometry.[75,76] Moreover, an analysis of the pre-edge region (Figure 6a inset) confirms the assignments of complexes **1** and **2**, with the first one showing a less pronounced pre-edge peak. This is due to the fact that in a square planar environment, the only contribution comes from $1s \rightarrow 3d$ electric quadrupole allowed transition, while, as the dihedral angle increases, the intensity of the peak increases for to the presence of an electric dipole transition due to mixing of 3d and 4p states.[76,77] Complex **3** shows a complete lack of the $1s \rightarrow 4p$ edge peak and a weak $1s \rightarrow 3d$ prepeak at a higher energy. This is indicative of an octahedral configuration since no d-p hybridization can occur and only electric quadrupole transitions are allowed by selection rules.[77] To further confirm the assignments of complexes **1**, **2**, and **3** their geometrical configuration was modeled and used to simulate the XANES

https://doi.org/10.1021/acs.jmedchem.4c00821
J. Med. Chem. XXXX, XXX, XXX−XXX

Table 4. Cu K-edge EXAFS Data Analysis for Complexes 1 to 5, Best Fit Results[a]

	shell 1				shell 2				shell 3				shell 4 (SS & MS)			
	N	*M*	*R*	σ^2	*A*	*M*	*R*	σ^2	*A*	*M*	*R*	σ^2	path	*M*	*R*	σ^2
sample			[Å]	×10² [Å²]			[Å]	×10² [Å²]			[Å]	×10² [Å²]			[Å]	×10² [Å²]
1	*N*	2	2.02(1)	0.26(1)	Cl	2	2.13(1)	2.2(2)	*N*	2	2.98(3)	0.78(4)	N_1-C_2	4	4.32(3)	1.2(5)
2	*N*	2	2.02(1)	0.52(2)	Br	2	2.38(1)	0.64(5)	*N*	2	3.02(3)	0.56(5)	N_1-C_2	4	4.34(5)	0.88(5)
3	*N*	4	2.01(1)	0.97(1)	O	2	2.43(1)	0.65(2)	*N*	4	2.99(2)	1.38(3)	$N_1-C_6-N_1$	8	4.20(3)	1.96(7)
4	*N*	2	1.99(1)	0.92(2)	P	1	2.24(1)	0.26(1)	*N*	2	3.01(3)	1.2(1)				
5	*N*	2	2.04(1)	0.97(3)	P	1	2.15(1)	0.38(1)	*N*	2	2.96(4)	1.4(2)	$P-C_3$	6	3.54(4)	0.16(3)

[a]For each sample, a fixed value of S_0^2 (0.9) was used, while the energy scale shift ΔE_0 was refined and fixed at 8.5 eV for complexes **1**, **2**, and **3**, and at 10.0 eV for complexes **4** and **5**. For each scattering contribution (single or multiple scattering) is reported the neighbor *N-type* (single scattering) or the neighbors (multiple scattering), multiplicity (*M*), average distance (*R*), and mean square relative displacement (σ^2). Multiplicities were fixed to the theoretical values.

Table 5. IC_{50} (μM) of L^{2Ad}, Copper Salts $CuCl_2$, $CuBr_2$ and $[Cu(CH_3CN)_4]PF_6$, Cu Compounds 1−5, and Cisplatin in Human Glioma Cell Lines (U87, T98, U251) and in the BV2 Microglial Cell Line[a]

	IC_{50} (μM)[b]			
compound	U87	T98	U251	BV2
L^{2Ad}	n.d.	>50	n.d.	n.d.
$CuCl_2$	>50	n.d.	>50	n.d.
$CuBr_2$	>50	>50	>50	n.d.
$[Cu(CH_3CN)_4]PF_6$	n.d.	n.d.	n.d.	n.d.
$[Cu(L^{2Ad})Cl_2]$ (**1**)	22.7 ± 3.2	16.1 ± 2.1	38.8 ± 3.2	48.5 ± 0.1
$[Cu(L^{2Ad})Br_2]$ (**2**)	39.6 ± 2.2	15.6 ± 1.9	38.0 ± 4.3	67.9 ± 5.2
$[Cu(L^{2Ad})_2]Br_2$ (**3**)	19.1 ± 1.7	9.0 ± 2.2	11.2 ± 0.5	28.0 ± 0.2
$[Cu(L^{2Ad})(PTA)]PF_6$ (**4**)	n.d.	32.5 ± 3.2	n.d.	n.d.
$[Cu(L^{2Ad})(PPh_3)]PF_6$ (**5**)	4.8 ± 1.2	4.3 ± 0.9	3.2 ± 1.1	17.8 ± 0.2
cisplatin	n.d.	>50	34.5 ± 6.6	2.9 ± 0.2

[a]The viability of cells was determined by the MTT assay after 72 h incubation with increasing concentrations (0−50 μM) of each compound. [b]IC_{50} values, the compound concentration required to inhibit 50% of cell viability, correspond to the mean ± standard error of the mean (S.E.M.) of at least three independent experiments. n.d., not determined.

region of these complexes using FEFF8.4[73] software with SCF-FMS calculations. The comparison between experimental data and simulated data is shown in Figure S8. In addition, the first derivatives of XANES spectra for complexes **1**−**5** and copper foil, Cu_2O, and CuO for comparison, are reported in Figure S9.

XANES spectra for Cu(I) complexes **4** and **5** (alongside metallic Cu for comparison) are shown in Figure 6b. Both complexes show no peaks in the pre-edge region, and the edge raising position is characteristic of Cu(I) valence (8980.0 and 8980.7 eV, respectively, for complexes **4** and **5**). The intense peak at 8982 eV is likely ascribed to the dipole-allowed photoelectron transitions $1s \rightarrow 4p$. The peak positions are coherent with the XANES shape and position and are consistent with Cu(I) sites, in a trigonal coordination geometry.[75] A key difference between the XANES of the two complexes arises right after the edge with complex **4** showing a secondary peak which is missed in complex **5**. As suggested by the literature this could be due to distortions in the local environment of the complex, which is adopting a T-shaped configuration instead of a trigonal planar geometry.[75,78]

Quantitative analysis of the EXAFS signals was achieved by fitting the k^2-weighted theoretical curves $k^2\chi_{th}$ to the raw experimental data $k^2\chi_{exp}$. The theoretical curves $\chi_{th}(k)$ were calculated as a sum of selected partial contributions χ_i, obtained by calculation of the photoelectron scattering amplitudes and phase functions using the FEFF8 software on already optimized DFT calculations of the complexes (as described in the *Structural Models* paragraph above). The χ_i were calculated using the standard EXAFS formula with Gaussian disorder approximation,[79−81] applying not linear least-squares procedure implemented in the program FiteEXA.[82] For each sample, the relevant single (SS) and multiple scattering (MS) contributions to the EXAFS signal were identified, and those with similar path length and amplitude were grouped. A trial-and-error procedure was performed with the aim of minimizing the free variables within each sample (definition of stochiometric constraints according to the structure of the complexes) and a detailed result of the fitting procedure is reported in Table 4.

All samples show a common bis pyrazol-1-yl bidentate ligand in the local environment of copper ions, which contributes to a few signals shared across complexes **1**−**5**, namely, the single scattering paths (SS) with the first and second Nitrogen neighbors ($Cu-N_1$ and $Cu-N_2$). Complexes **1** and **2** show the characteristic signals of the halogen neighboring atoms Cu−Cl and Cu−Br respectively, as well as the multiple scattering contribution $Cu-N_1-C_2$ (predominant only in this couple). Complex **3** shows the Cu−O scattering path from the apical Oxygen atoms, as well as multiplicities coherent with what was observed in XRD, with two bis pyrazol-1-yl ligands in the plane of the octahedron. Additionally, Complex **3** shows an intense $Cu-N_1-C_5/C_6-N_1$ MS contribution amplified by the almost collinear configuration (forward scattering effect). Complexes **4** and **5** instead also show signals coming from their phosphine ligands, PTA and PPh_3 respectively, with common scattering paths such as Cu−P (SS). Complex **5** also shows a relevant $Cu-P-C_3$ MS contribution. The shell resolved fit of the extended region

https://doi.org/10.1021/acs.jmedchem.4c00821
J. Med. Chem. XXXX, XXX, XXX−XXX

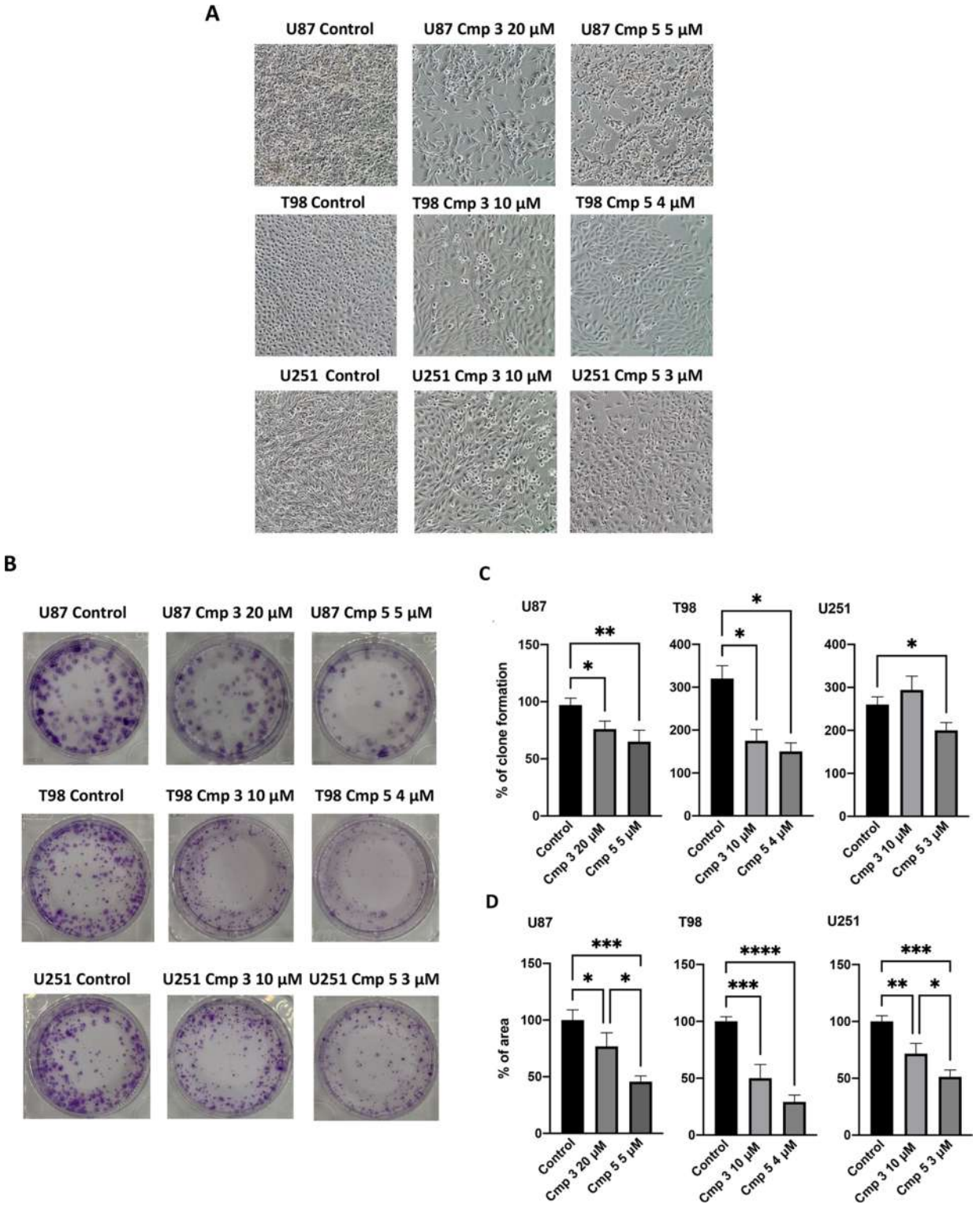

Figure 7. Effect of Cu compounds **3** and **5** on glioma cell growth. (A) Representative images of glioma cells treated with compounds **3** and **5** or with vehicle (control) for 72 h. Magnification 10×. (B) Colony formation observed in cells treated for 14 days as above-described, then fixed with 4% paraformaldehyde and stained with 0.2% crystal violet. Colonies were photographed and counted under the microscope. (C) Bar charts showing the decrease in the number of colonies after incubation with Cu compounds. (D) Bar charts showing the decrease in the percentage of colony area after incubation with Cu compounds. Results are the mean ± SEM of at least three independent experiments. * $p < 0.05$; ** $p < 0.01$; *** $p < 0.001$; **** $p < 0.0001$.

(EXAFS) for complexes **1**−**5** is reported in Figure S10. The results of the EXAFS analysis are consistent with XRD and DFT models and contribute to providing a reliable description of the average local atomic structure around Cu sites in these complexes.

2.6. Biological Studies. *2.6.1. Effect of Cu Complexes on Glioma Cell Viability.* The new complexes **1**−**5** and the

https://doi.org/10.1021/acs.jmedchem.4c00821
J. Med. Chem. XXXX, XXX, XXX−XXX

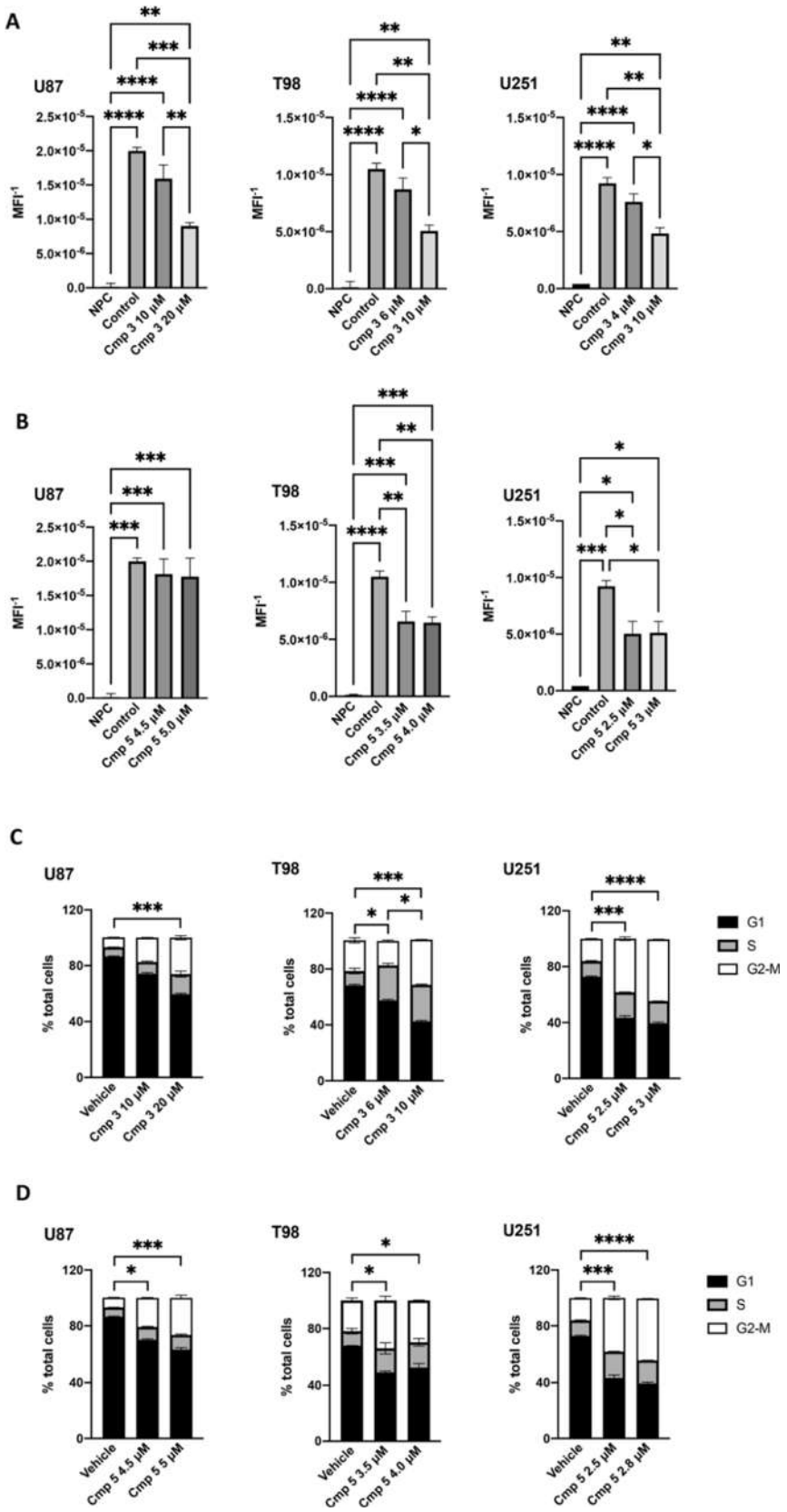

Figure 8. Effect of Cu compounds **3** and **5** on glioma cell proliferation. (A, B) Glioma cells were stained with CFSE and then seeded and cultured with compounds **3**, **5** or with vehicle for 72 h. Then, cells were harvested and the CFSE fluorescence signal was measured. Statistical analysis is calculated using the inverse of CFSE MFI values (MFI−1). NPC, nonproliferative control. (C, D) Cells were treated for 72 h with different doses of compounds **3** and **5**. The cell cycle profile was assessed by flow cytometry following PI staining. The frequency of cell cycle phases for each condition was shown. Results are the mean ± SEM of at least three independent experiments. * $p < 0.05$; ** $p < 0.01$; *** $p < 0.001$; **** $p < 0.0001$.

https://doi.org/10.1021/acs.jmedchem.4c00821
J. Med. Chem. XXXX, XXX, XXX−XXX

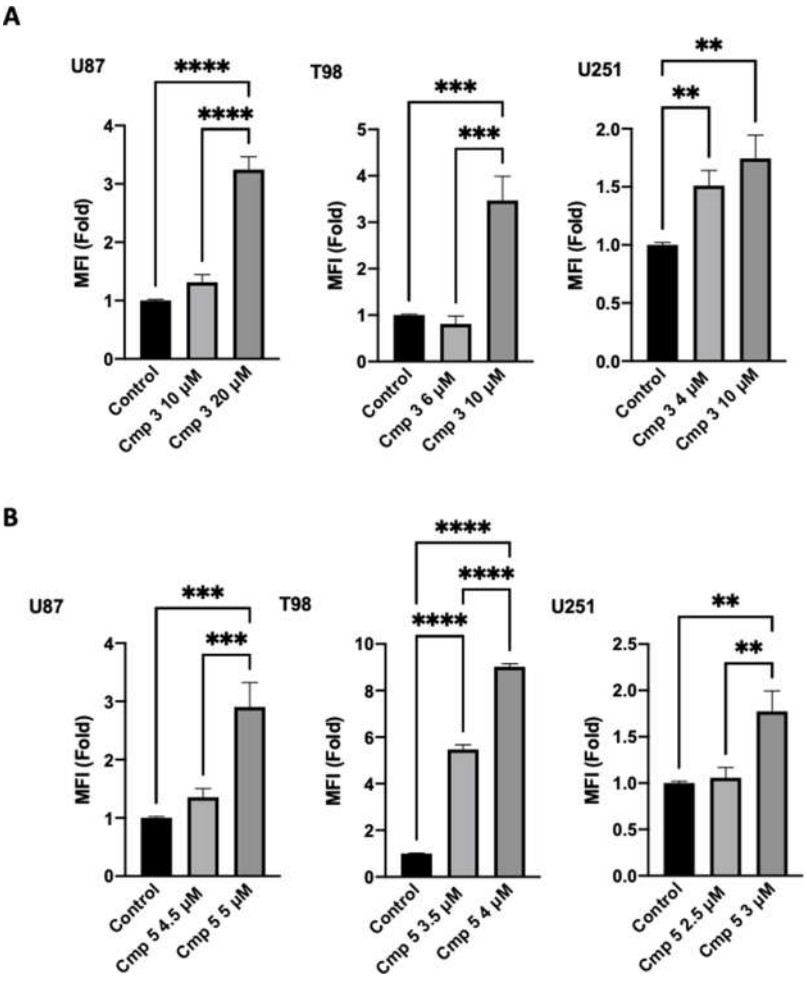

Figure 9. Effect of Cu compounds **3** and **5** on glioma cell death. (A, B) Glioma cells were cultured with compounds **3**, **5** or with vehicle for 72 h. Flow cytometric analysis was performed by PI staining. The mean fluorescence intensity (MFI) values of treated cells were normalized to those of the vehicle (control). Results are the mean ± SEM of at least three independent experiments. * $p < 0.05$; ** $p < 0.01$; *** $p < 0.001$; **** $p < 0.0001$.

corresponding uncoordinated ligand L^{2Ad} were evaluated for their ability to affect the cell viability of three different glioblastoma cell lines (U87, T98, U251). The IC_{50} values, obtained after 72 h exposure by 3-[4,5-dime-thylthiazole-2-yl]-2,5-dimethyltetrazolium bromide (MTT) assay, are reported in Table 5 together with those of the chemotherapeutic drug cisplatin and copper salts $CuCl_2$, $CuBr_2$ and $[Cu(CH_3CN)_4]$-PF_6, included for useful comparison.

From data analysis, it emerges that ligand L^{2Ad} and copper salts $CuCl_2$, $CuBr_2$, and $[Cu(CH_3CN)_4]PF_6$, showed negligible toxicity toward the studied cell lines. While complex **4** decreased viability only on the T98 cell line (IC_{50} = 32.5 μM), complexes **1**, **2**, **3**, and **5** displayed cytotoxicity toward all three cell lines in a dose-dependent manner (Table 5 and Figure S11). Interestingly, the three lines proved to be more susceptible to the studied Cu complexes than to cisplatin. Among the Cu(II) complexes, **3** displayed the greatest toxicity, with an IC_{50} lower than 20 μM. The most promising cytotoxic profile within this series was shown by the Cu(I) complex $[Cu(L^{2Ad})(PPh_3)]PF_6$ (**5**), with IC_{50} values in the low micromolar range. This result allows us to hypothesize that the lipophilicity of the PPh_3 coligand might confer to the complex the ability to cross plasma membranes, markedly affecting cell viability.

Another interesting result was observed by evaluating the ability of the new Cu complexes to affect the viability of the primary microglial BV2 cells used to explore their toxicity in normal cells. Indeed, unlike cisplatin, complexes **1**−**5** showed significantly lower toxicity in nontumor BV2 microglial cells than in the glioblastoma cell lines (Table 5, Figure S12) suggesting good biocompatibility profiles.

*2.6.2. Evaluation of Compounds **3** and **5** on Glioma Cell Growth.* Encouraged by the results presented above, we further investigated the bioactivity of compounds **3** and **5**. First, we examined their influence on cellular morphological changes by phase-contrast microscopy. Figure 7A shows that untreated control cells were able to proliferate and cover the entire plate, while compound **3** or **5** reduced tumor cell numbers and caused some of them to take on a spherical shape, indicating that the compounds exert cytotoxic action against glioblastoma cells.

In addition, the confocal microscopy imaging technique was used to evaluate the Cu complexes' cellular uptake exploiting the fluorescent probe BioTracker Green Copper, which specifically detects Cu(I) ions. The cell-permeable Green Copper has almost no fluorescence; however, it fluoresces upon reaction with intracellular Cu(I). As shown in Figure S13, cell-associated fluorescence is not detected in control

https://doi.org/10.1021/acs.jmedchem.4c00821
J. Med. Chem. XXXX, XXX, XXX−XXX

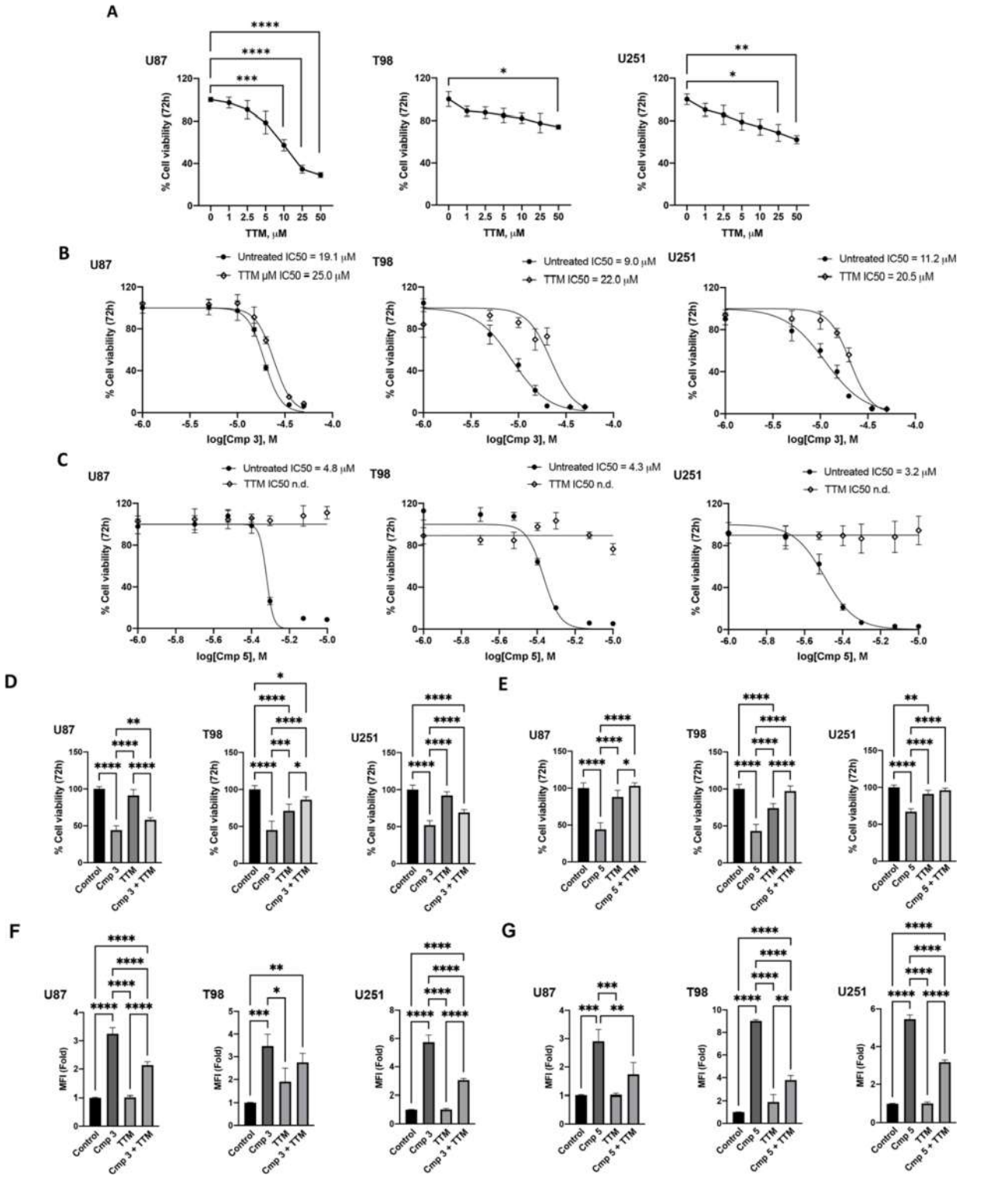

Figure 10. Role of Cu in the decrease in viability induced by compounds **3** and **5**. (A) Cell viability was assessed after treating the glioma cell lines with TTM. (B, C) Cell viability was assessed in the three cell lines after receiving a combination of different doses of compound **3** or **5** with TTM at the specific IC_{25} dose for each cell line. IC_{50} represents the drug concentration (μM) required to inhibit 50% net cell viability. (D, E) Cell viability was assessed after receiving a combination of Cu compounds at IC_{50} doses and TTM as above-described. (F, G) Cells treated as above-described were analyzed by flow cytometry for PI staining. The mean fluorescence intensity (MFI) values of treated cells were normalized to those of the vehicle (control). Data shown are expressed as mean ± SEM of three separate experiments. * $p < 0.05$; ** $p < 0.01$; *** $p < 0.001$; **** $p < 0.0001$.

cells, whereas treatment with complexes **3** and **5** reveals an intracellular signal supporting the cellular uptake of both compounds and, in the case of complex **3**, the intracellular reduction of Cu(II) to Cu(I).

https://doi.org/10.1021/acs.jmedchem.4c00821
J. Med. Chem. XXXX, XXX, XXX−XXX

Moreover, the inhibitory effect of **3** and **5** on the proliferative ability of glioma cells was determined via a colony formation assay. Cells were seeded into a 6-well cell culture plate, treated with an IC_{50} dose for 14 days, and then stained with crystal violet. As shown in Figure 7B and C, treatment with compound **3** resulted in significant suppression of cell colony formation in U87 and T98, whereas compound **5** induced an even greater decrease in the number of colonies and was also effective in U251 cells. Furthermore, as indicated by the decrease in the percentage of colony area, cells treated with both compounds formed smaller colonies compared to the control group. These results demonstrate that compounds **3** and **5** inhibit the growth of glioma cells and that the inhibitory effect persists for a significant period of time.

Based on the colony formation assay, we further investigated the role of compounds **3** and **5** in cell proliferation. The Cu compounds were used at concentrations corresponding to IC_{50} and IC_{25} (the compound concentration required to inhibit 25% of cell viability) in all subsequent experiments. To this purpose we exploited the ability of CFSE, a fluorescent cell staining dye, to be retained within cells and divided between daughter cells during proliferation. As shown in Figures 8A, B, and S14, compound **3** was able to significantly reduce the proliferation of the three cell lines at IC_{50} doses than in untreated cultures, whereas compound **5** was effective in T98 and U251 cells. In order to further study the effect of compounds **3** and **5** on cell growth, we also evaluated the cell cycle arrest. Figures 8C, D, and S15 show that the cell cycle of vehicle-treated cells was G0/G1 dominant, but the cell cycle began to arrest when cells were treated with compounds **3** or **5**. Indeed, after 72 h of treatment, glioma cells accumulated in the G2-M phase compared to vehicle-treated cells. The significant increase in the cell number in the G2-M phase was accompanied by a decrease in the number of cells in G1. These findings indicate that both Cu complexes inhibited the proliferation of glioma cells in a concentration-dependent manner.

To better understand the effects of compounds **3** and **5** on cell viability, after 72 h of treatment, cell death was measured by flow cytometry using PI staining. Given that PI only enters the cells with compromised permeability of the membrane, it stains only dead and late apoptotic cells. As shown in Figures 9 and S16, when cells were treated with Cu compounds at IC_{50} dose, the fluorescence increased and the percentages of cell death were significantly higher than in the control groups. However, in general, there were no significant differences when cells were exposed to lower IC_{25} concentrations, suggesting that this dose mainly has an antiproliferative effect.

*2.6.3. Evaluation of the Effect of Compounds **3** and **5** on Glioma Cells Viability in the Presence of Cu Chelator Tetrathiomolybdate (TTM).* To evaluate the involvement of copper in the cytotoxic activity of compounds **3** and **5**, we utilized Cu chelator TTM alone (Figure 10A) or in combination with Cu compounds (Figure 10B–G). MTT assays revealed that the cotreatment with TTM partially reduced the ability of compound **3** (Figure 10B, D, F) to induce cell death and completely abolished the activity of compound **5** (Figure 10C, E, G), confirming the critical role of the metal.

*2.6.4. Effect of Cu Complexes **3** and **5** on the Intracellular ROS Production in Glioma Cells.* Although Cu is a biologically vital micronutrient, it can be toxic depending upon the concentration and exposure.[83] The principal mechanism of action of transition metal ions likely involves the formation of hydroxyl radical, superoxide ion, and other ROS.[84−86] Copper can perform a redox cycling reaction that induces the formation of ROS. Many studies showing the ability of Cu ions to participate in ROS demonstrated a resulting alteration of the structure and/or function of biomolecules.[87,88] Thus, ROS levels were evaluated in the three cell lines treated with Cu complexes **3** and **5**. To this aim the cell permeable H2DCFDA was employed. It is cleaved by intracellular esterases and oxidized by various ROS to green fluorescent DCF. The results indicated that compared to the control group, the ROS production levels are significantly increased after treatment with compound **3** at IC_{50} doses, whereas compound **5** could induce a statistically significant increase already at the IC_{25} dose (Figure 11 A, B).

Among the reactive species, the hydroxyl radical is considered as the most powerful oxidizing agent able to initiate oxidative damage to almost all cellular components.[89−91] It also induces oxidation of bases and DNA strand breaks.[92−95] The nucleosomal histone protein H2AX is specifically phosphorylated (γH2AX) adjacent to DNA double-strand breaks (DSBs) and is used for quantifying this type of damage. In Figure 11 C,D γH2AX staining showed an increased fluorescence of samples, suggesting that an enhanced generation of ROS leads to DNA damage and death. Our data was supported by several studies demonstrating that oxidative damage induced by ROS plays a key role in Cu complexes toxicity.[96]

*2.6.5. Effect of Cu Compounds **3** and **5** in the Killing Effect of TMZ on Glioma Cell Lines.* Since its approval by the US FDA in 2005, TMZ has been used in the first-line chemotherapy regimen for GBM and, despite numerous studies, patient survival has not substantially improved, due to the emergence of treatment resistance.[97] Several cell lines have been extensively studied to understand the molecular mechanisms causing TMZ resistance in GBM. However, this phenomenon remains insufficiently understood as multiple molecular mechanisms are involved.[97−100] Given that numerous factors make the brain vulnerable to oxidative stress and that Cu overload stimulates damaging ROS generation mediated by Fenton reactions,[101] we aimed to increase the cytotoxic effect of TMZ by administering it together with the Cu complexes. Thus, glioma cells were treated with TMZ alone or in combination with compound **3** or **5** at IC_{25} doses. The combination revealed that the addition of Cu compounds enhanced the ability of TMZ to induce glioma cell death based on IC_{50} values (Figure 12). In particular, compound **5** was able to achieve more significant results, even halving the effective TMZ dose. These findings revealed that Cu compounds, used at a nontoxic dose, are able to enhance the killing effect of TMZ on glioma cells. This effect is linked to an increase in the level of ROS production and cell death. Indeed, IC_{25} doses of compounds **3** or **5** by themselves did not increase ROS production, which, interestingly, was increased when used in combination with TMZ. Similar results were obtained with the incorporation of PI, a sign of cell death (Figure S17).

Moreover, we underline the ability of Cu complexes to increase the efficacy of TMZ despite the different sensitivities of the three cell lines analyzed. Thus, there would be great advantages in therapy because the drug could be administered to patients at lower concentrations and with fewer side effects, despite the variability in response to traditional drugs.

https://doi.org/10.1021/acs.jmedchem.4c00821
J. Med. Chem. XXXX, XXX, XXX−XXX

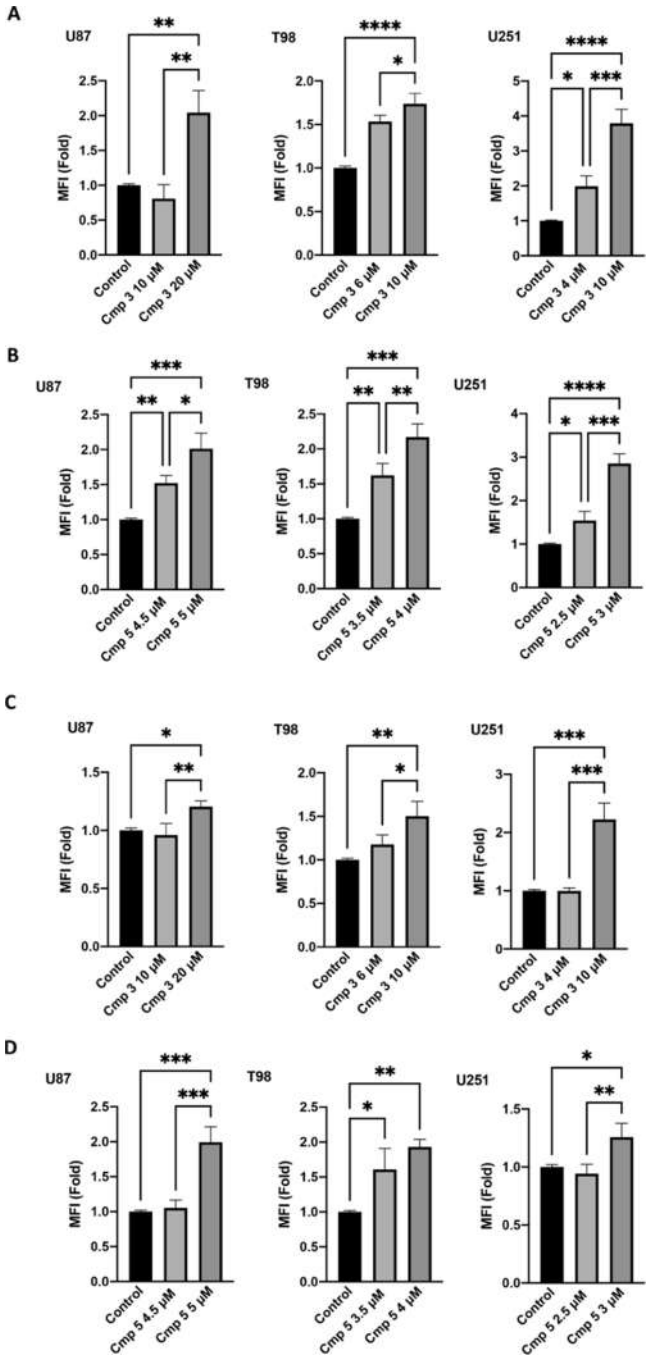

Figure 11. Effect of Cu compounds **3** and **5** on ROS production in glioma cell lines. (A, B) ROS generation in glioma cell lines treated with compounds **3**, **5**, or with vehicle for 72 h. Cells were stained with DCFDA before flow cytometric analysis. Data are expressed as fold. The mean fluorescence intensity (MFI) values of treated cells were normalized to those of control. (C, D) Cytofluorimetric analysis of glioma cells treated as above-described and labeled with anti-γH2AX antibody. The mean fluorescence intensity (MFI) values of treated cells were normalized to those of control. Results are the mean ± SEM of at least three independent experiments. * $p < 0.05$; ** $p < 0.01$; *** $p < 0.001$; **** $p < 0.0001$.

3. CONCLUSIONS

In the present study, the bifunctional species bis(3,5-dimethylpyrazol-1-yl)-acetate was conjugated to the known drug amantadine to obtain the new ligand L^{2Ad}, which was used as a chelator for the synthesis of new Cu(II) complexes **1**-**3** and Cu(I) complexes **4** and **5**. The hydrophilic 1,3,5-triaza-7-phosphaadamantane and the lipophilic triphenylphosphine were used for the synthesis of Cu(I) complexes, to stabilize Cu in +1 oxidation state. All complexes were fully characterized in the solid state and in solution. SR-XPS and NEXAFS data analysis allowed assessment of the molecular and electronic structure stability of the ligands in both Cu(II) and Cu(I) coordination compounds, confirming the preservation of the L^{2Ad} and phosphane (either PPh_3 or PTA) coligands. XAS studies allowed, by observing the XANES spectra and comparing them with literature data, to ascertain the copper ion oxidation state confirming the proposed chemical structures; on the other hand, the analysis of the extended EXAFS region provided information about the local geometry of ligands around the copper center. For complex **3** XAS results are in excellent agreement with XRD findings. The single-crystal XRD analyses revealed the molecular structure of complex **3**, where the stoichiometric ligand-to-metal 2:1 ratio promotes the entry of a second L^{2Ad} unit into the metal coordination sphere, in place of the two bromide anions which instead participate in the Cu(II) donor set of complex **2**. The two ligand molecules coordinate copper, forming a bis-tridentate, *trans*-facial distorted octahedral environment. Notably, the two bromide counterions, although getting involved in a hydrogen bond network with cocrystallized water molecules, enjoy an unusual degree of positional freedom at the crossing of a 2-fold proper rotation axis with a mirror plane and thus assume disordinate positions in the unit cell. All the complexes and the corresponding uncoordinated ligand were evaluated for their ability to affect the cell viability of three different GBM cell lines (U87, T98, U251). In particular, Cu(II) complex **3** and especially Cu(I) complex **5** decreased the viability of all the studied cell lines, with IC_{50} values in the low micromolar range and efficacy significantly higher than that of the reference drug cisplatin. They affected GBM cell growth, proliferation, and death. Moreover, unlike cisplatin, they showed significantly lower toxicity in nontumor microglial BV2 cells. Interestingly, the effects of **3** and **5** on glioma cell viability were prevented by treatment with the Cu chelator TTM, strongly suggesting the involvement of copper in their cytotoxic activity. The results also indicated that both complexes were able to increase ROS production levels, leading to DNA damage and death. A more and more fascinating finding was obtained by using nontoxic doses of **3** or **5** in combination with TMZ, the first-line chemotherapy agent for GBM treatment. Indeed, both compounds strongly enhance the TMZ-killing effect on glioma cells. This effect is linked to an increase in ROS production and cell death. The therapeutic advantage of this combination could lie in the reduction of TMZ doses to patients, thereby limiting the adverse effects of this drug. Considering the suggested role of copper in enhancing the bioavailability of MTIC derived from TMZ,[18] the interaction between copper complexes **3** or **5** and TMZ would deserve to be investigated. Moreover, due to their interesting biological profiles, complexes **3** and especially **5** deserve to be further studied, to shed light on the mechanism of their antitumor activity and to better evaluate their potential application in the treatment of GBM.

4. EXPERIMENTAL SECTION

4.1. Chemistry. *4.1.1. Materials and General Methods.* All reagents used for the synthesis of ligands and complexes were purchased from Sigma-Aldrich and used without further purification.

https://doi.org/10.1021/acs.jmedchem.4c00821
J. Med. Chem. XXXX, XXX, XXX−XXX

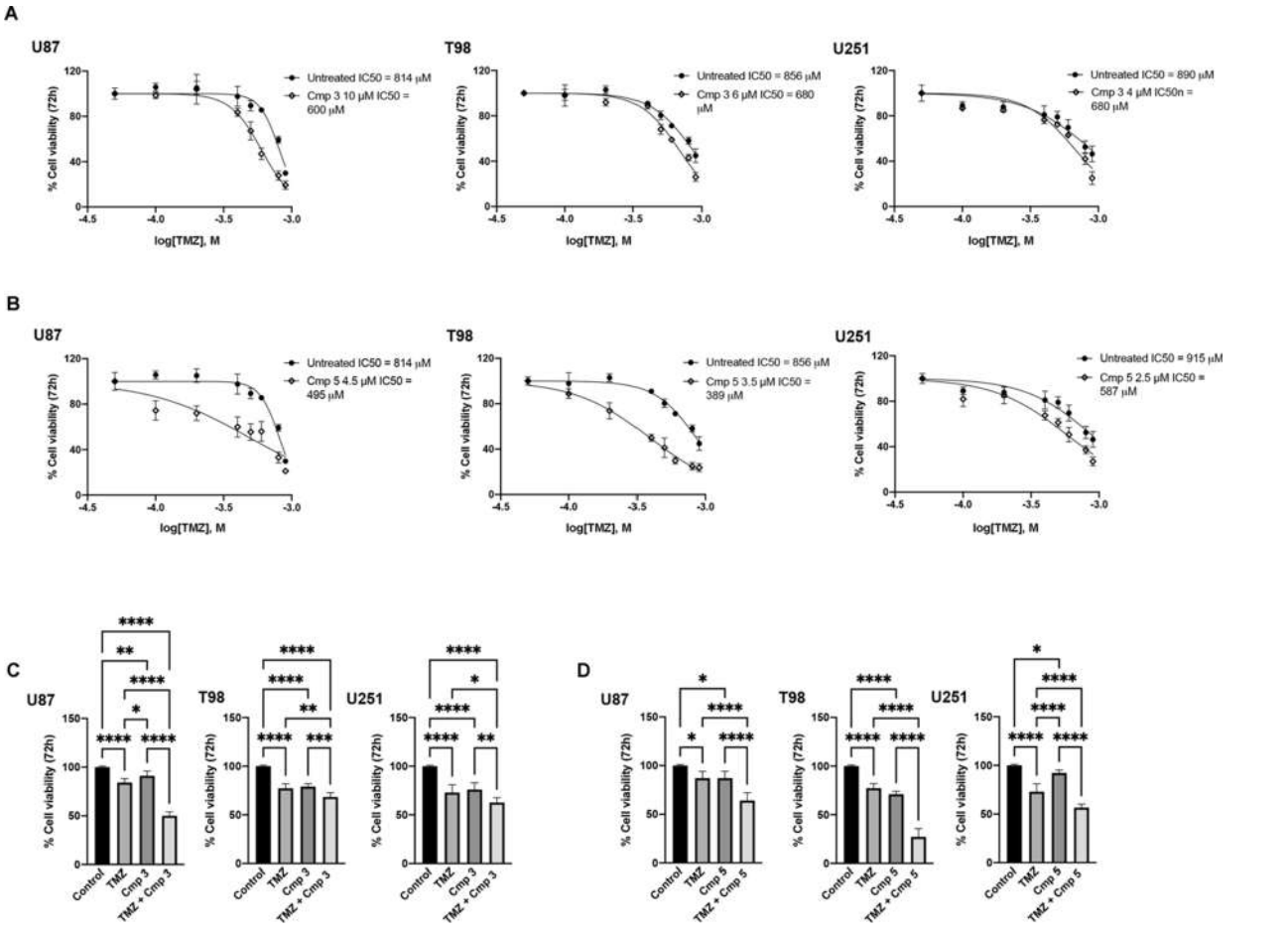

Figure 12. Role of Cu complexes **3** and **5** in increasing the TMZ response. (A, B) Cell viability was assessed after treating the glioma cell lines with increasing concentration of TMZ in combination with IC_{25} doses of compounds **3** or **5**. The values of IC_{50} shown represent the TMZ concentration, alone or in combination with Cu complexes, required to inhibit 50% net cell viability. (C, D) Bar graph represents the response in terms of cellular viability to treatment with TMZ (600 μM) and compounds **3** and **5** at IC_{25} doses. Data shown are expressed as mean ± SEM of three separate experiments. * $p < 0.05$; ** $p < 0.01$; *** $p < 0.001$; **** $p < 0.0001$.

Elemental analyses (C, H, N, S) were performed in-house with a Fisons THERMO Fisher Flash 2000 instrument. Melting points were taken on an SMP3 Stuart Scientific Instrument. IR spectra were recorded from 4000 to 200 cm^{-1} with a PerkinElmer Frontier FT-IR Instrument. IR annotations used: br = broad, m = medium, mbr = medium broad, sh = shoulder, s = strong, vs = very strong, w = weak, wbr = weak broad. ^{1}H,^{31}P, and ^{13}C NMR spectra were recorded on an Ascend 500 Bruker spectrometer (500.1 MHz for ^{1}H, 202.5 MHz for ^{31}P, and 125.8 MHz for ^{13}C). Chemical shifts, in parts per million, for ^{1}H NMR spectra are relative to internal standard Me_4Si. ^{31}P NMR chemical shifts were referenced to an 85% H_3PO_4 standard. The ^{31}P NMR chemical shifts were acquired with ^{1}H decoupling. NMR annotations used: s = singlet, d = doublet, br = broad, m = multiplet, sbr = singlet broad, dd = doublet of doublets, q = quartet, sept = septet, t = triplet. Electrospray ionization-mass spectra (ESI-MS) were obtained in positive- and negative-ion mode on a Series 1100 MSD detector HP spectrometer using a methanol and acetonitrile mobile phase. The compounds were added to reagent grade CH_3OH, CH_3CN, CH_3CH_2OH, or H_2O to give solutions of approximate concentration of 0.1 mM. These solutions were injected (1 μL) into the spectrometer via an HPLC HP 1090 Series II fitted with an autosampler. The pump delivered the solutions to the mass spectrometer source at a flow rate of 300 μL min^{-1}, and nitrogen was employed both as a drying and nebulizing gas. Capillary voltages were typically 4000 and 3500 V for the positive- and negative-ion modes, respectively. Confirmation of all major species in this ESI-MS study was aided by a comparison of the observed and predicted isotope distribution patterns, the latter calculated using the IsoPro 3.0 computer program. The purity of the novel compounds was determined by combustion analysis and is >95%.

The spectroscopic characterization of the ligand L^{2Ad} and the complexes **1**−**5** (FT-IR, ^{1}H-, $^{13}C\{^{1}H\}$- and $^{31}P\{^{1}H\}$ spectra) has been reported in the Supporting Information (Figures S18−S40).

4.1.2. Synthesis of L^{2Ad}. DIPEA (0.294 g, 2.280 mmol) was added to a stirred solution of amantadine (0.157 g, 1.040 mmol) in DMF (10 mL). A solution of $L^{2}H$ (0.200 g, 1.040 mmol) and TBTU (0.334 g, 1.040 mmol) in DMF (10 mL) was then added dropwise, and the resulting solution was stirred for 20 h at room temperature. After dilution with brine (30 mL), the mixture was extracted with ethyl acetate (2 × 30 mL) and the organic phase was washed with distilled water (5 × 20 mL), dried over anhydrous Na_2SO_4 and evaporated. The residue was purified by flash chromatography eluting with cyclohexane/ethyl acetate (5:5) to give the ligand L^{2Ad} as a white solid in 86% yield. Mp: 149−152 °C. Solubility: CH_3CN, $CHCl_3$, CH_2Cl_2, acetone, THF and DMSO. FT-IR (cm^{-1}): 3324w, 3300w (N−H); 3080wbr, 3029wbr, 2905s, 2848m (C−H); 1671vs (C═O); 1554s (C═C/C═N); 1493w, 1449s, 1418m, 1370m, 1360s, 1339s, 1320m, 1310m, 1293s, 1256w, 1278s, 1263m, 1243m, 1216w, 1188w, 1121mbr, 1103m, 1092s, 1063m, 1026m, 999w, 988w, 941wbr, 920w, 894m, 861w, 831s, 820m, 785s, 773s, 757s, 731m, 715m. ^{1}H NMR ($CDCl_3$, 293 K): δ 1.45−2.40 (m, 15H, CH_{ADM} and CH_3), 5.84 (t, 2H, 4-CH_{pz}), 6.63 (s, 1H, α−CH), 7.46 (s, 1H, NH). $^{13}C\{^{1}H\}$-NMR ($CDCl_3$, 293 K): 11.4, 13.6 (CH_3); 29.4, 36.3, 41.1, 52.6 (CH_{ADM}); 71.6 (α-CH); 106.9 (4-CH_{pz}); 141.1 (5-C_{pz}); 149.2 (3-C_{pz}); 162.9 (C═O). ESI-MS(+) (major positive ions, CH_3CN), m/z

https://doi.org/10.1021/acs.jmedchem.4c00821
J. Med. Chem. XXXX, XXX, XXX−XXX

(%): 382 (60) $[L^{2Ad} + H]^+$, 404 (100) $[L^{2Ad} + Na]^+$, 420 (50) $[L^{2Ad} + K]^+$, 785 (30) $[2L^{2Ad} + Na]^+$. Elemental Analysis (%) calcd for $C_{22}H_{31}N_5O$: C 69.26, H 8.19, N 18.36; found: C 69.53, H 8.01, N 18.11.

4.1.3. Synthesis of [Cu(L^{2Ad})Cl_2] (1). The ligand L^{2Ad} (0.500 mmol, 0.190 g) was added to a solution of copper chloride (0.500 mmol, 0.085 g) in CH_3CN (30 mL). The reaction was stirred for 24 h at room temperature. The precipitate was filtered, washed with CH_3OH, and dried under reduced pressure to give the yellow complex [Cu(L^{2Ad})Cl_2] in 80% yield. Mp: 283−285 °C. Solubility: CH_3OH, CH_3CH_2OH, CH_2Cl_2, $CHCl_3$, CH_3CN, DMSO, and Acetone. FT-IR (cm^{-1}): 3208wbr (N−H); 3060w, 2913m, 2853w (C−H); 1664vs (C═O); 1646sh, 1558s, 1487w, 1457m, 1417m (C═C/C═N); 1394m, 1378m, 1360m, 1354sh, 1344sh, 1310s, 1268w, 1250sh, 1237m, 1191w, 1133w, 1087m, 1051m, 999mbr, 940w, 924m, 893w, 877m, 831m, 789m, 775w, 703m, 651s, 623wbr, 594wbr, 573s, 545wbr, 526wbr, 488m, 471wbr, 453m, 420wbr, 411wbr, 378m, 359m, 324mbr, 302m; 280vs (Cu−Cl); 264s, 253m, 247s, 229s, 214s, 202vs ESI-MS(+) (major positive ions, CH_3CN), *m*/*z* (%): 135 (20) $[CuCl_2 + H]^+$, 413 (100) $[Cu(L^{2Ad})_2]^{2+}$, 479 (15) $[Cu(L^{2Ad}) + Cl]^+$. Elemental Analysis (%) calcd for $C_{22}H_{33}Cl_2CuN_5O_2$: C 49.48, H 6.23, N 14.12; found: C 49.36, H 6.17, N 14.58.

4.1.4. Synthesis of [Cu(L^{2Ad})Br_2] (2). The ligand L^{2Ad} (0.500 mmol, 0.190 g) was added to a copper(II) bromide (0.500 mmol, 0.110 g) solution in CH_3CN (20 mL). The reaction was stirred for 20 h at room temperature and then for 4 h at reflux. The precipitate was filtered and dried under reduced pressure to give the dark purple complex [Cu(L^{2Ad})Br_2] in 44% yield. Mp: 248−250 °C. Solubility: DMSO, CH_3OH, and CH_3CH_2OH. FT-IR (cm^{-1}): 3194wbr, 3053wbr, 2983w, 2963w, 2909m, 2851w (C−H); 1670sh, 1659sh, 1634vs (C═O); 1558s, 1455m, 1417m (C═C/C═N); 1400m, 1389m, 1372m, 1362m, 1353m, 1344w, 1325w, 1307s, 1268w, 1243m, 1129w, 1104w, 1087m, 1040m, 1003w, 993w, 982w, 926w, 889w, 871w, 826m, 817m, 796m, 776w, 704w, 666w, 648m, 637m, 620wbr, 588wbr, 575m, 543w, 486m, 460m, 427w, 413w, 387w, 366w, 337w, 309w, 295w, 285m, 274m, 258m, 250sh; 242vs, 232vs (Cu−Br); 208s. ESI-MS(+) (major positive ions, CH_3OH), *m*/*z* (%): 413 (100) $[Cu(L^{2Ad})_2]^{2+}$, 525 (10) $[Cu(L^{2Ad})Br]^+$, 906 (15) $[Cu(L^{2Ad})_2Br]^+$. ESI-MS(−) (major negative ions, CH_3OH), *m*/*z* (%): 304 (100) $[CuBr_3]^-$. Elemental Analysis (%) calcd for $C_{22}H_{31}Br_2CuN_5O$: C 43.68, H 5.17, N 11.58; found: C 44.14, H 5.18, N 12.04.

4.1.5. Synthesis of [Cu(L^{2Ad})$_2Br_2$] (3). The ligand L^{2Ad} (0.500 mmol, 0.190 g) and copper(II) bromide (0.250 mmol, 0.056 g) were dissolved in CH_3CN (20 mL) and the reaction was stirred for 24 h at reflux. A precipitate was formed, which was filtered and dried under reduced pressure to give the light green complex [Cu(L^{2Ad})$_2Br_2$] in 76% yield. Mp: 243−245 °C. Solubility: CH_3OH, CH_2Cl_2, $CHCl_3$, CH_3CN, and DMSO. FT-IR (cm^{-1}): 3181wbr (N−H); 3135w, 2949sh, 2935sh, 2901vs, 2850s, 2812s (C−H); 1667vs (C═O); 1586vs, 1560vs, 1414s (C═C/C═N); 1393vs, 1373vs, 1354vs, 1340s, 1311vs, 1266m, 1245vs, 1185m, 1133m, 1118w, 1111w, 1101w, 1050s, 995m, 941w, 921s, 888m, 873s, 814vs, 806vs, 785vs, 775sh, 702m, 653vs, 642s, 571vs, 535w, 505w, 487s, 457m, 448m, 412m, 378m, 360m, 339w, 318m, 302m; 281vs, 275s, 264s (Cu−Br); 255sh, 245m, 233s, 224s. ESI-MS(+) (major positive ions, CH_3CN), *m*/*z* (%): 413 (100) $[Cu(L^{2Ad})_2]^{2+}$, 525 (10) $[Cu(L^{2Ad})Br]^+$, 824 (95) $[2L^{2Ad} + Na + CH_3CN]^+$, 906 (20) $[Cu(L^{2Ad})_2Br]^+$. ESI-MS(−) (major negative ions, CH_2Cl_2/CH_3CN), *m*/*z* (%): 304 (20) $[CuBr_3]^-$. Elemental Analysis (%) calcd for $C_{44}H_{62}Br_2CuN_{10}O_2$: C 53.58, H 6.34, N 14.20; found: C 53.19, H 6.18, N 13.89.

4.1.6. Synthesis of [Cu(L^{2Ad})(PTA)]PF_6 (4). 1,3,5-Triaza-phosphaadamantane (1.000 mmol, 0.157 g) was added to an acetonitrile solution (30 mL) of tetrakis(acetonitrile)copper(I)-hexafluorophosphate (0.500 mmol, 0.186 g). The reaction was stirred for 3 h at room temperature, and then the ligand L^{2Ad} (0.500 mmol, 0.190 g) was added. The reaction was stirred for 20 h at room temperature and at reflux for 3 h. The solvent was evaporated at reduced pressure, giving a white solid, which was washed with diethyl ether (30 mL) and dried under reduced pressure to give the complex [Cu(L^{2Ad})(PTA)]PF_6 in 92% yield. Mp: 180−183 °C. Solubility: CH_3CN, DMSO. FT-IR (cm^{-1}): 3228wbr (N−H); 3067wbr, 2907w, 2825wbr (C−H); 1672w (C═O); 1561w, 1528s, 1450w, 1417m (C═C/C═N); 1361w, 1293w, 1242m, 1104m, 1041w, 1014m, 970s, 948m, 894w; 835vs (PF_6); 743m, 593m, 582s, 556vs, 480m, 448m. ^1H NMR (CD_3CN, 293 K): δ 1.67−2.39 (m, 27H, CH_{ADM} and CH_3), 4.13 (s, 6H, NCH_2N), 4.50−4.62 (dd, 6H, NCH_2P), 6.03 (s, 2H, 4−CH_{pz}), 6.58 (s, 1H, α−CH). $^{13}C\{^1H\}$-NMR (DMSO, 293 K): δ 11.1, 14.4 (CH_3); 29.1, 36.1 (CH_{ADM}); 50.6, 51.8, 72.3 (CH_{PTA}); 107.0 (4-CH_{pz}); 142.5 (5-CH_{pz}); 150.2 (3-CH_{pz}); 165.0 (*C*═O). $^{31}P\{^1H\}$-NMR (CD_3CN, 293 K): δ −144.62 (sept, J_{F-P} = 706 Hz), −94.35 (sbr). ESI-MS(+) (major positive ions, CH_3CN), *m*/*z* (%): 145 (60) $[Cu + 2CH_3CN]^+$, 158 (50) $[PTA + H]^+$, 261 (40) $[Cu(PTA) + CH_3CN]^+$, 485 (70) $[Cu(L^{2Ad}) + CH_3CN]^+$, 601 (100) $[Cu(L^{2Ad})(PTA)]^+$. ESI-MS(−) (major negative ions, CH_3CN), *m*/*z* (%): 145 (100) $[PF_6]^-$. Elemental Analysis (%) calcd for $C_{28}H_{43}CuF_6N_8OP_2$ (%): C 45.01, H 5.80, N 15.00; found: C 45.41, H 5.97, N 15.30.

4.1.7. Synthesis of [Cu(L^{2Ad})(PPh_3)]PF_6 (5). Tetrakis(acetonitrile)-copper(I)hexafluorophosphate (0.500 mmol, 0.186 g) and triphenylphosphine (1.000 mmol, 0.260 g) were dissolved in CH_3CN (30 mL) and the reaction was stirred for 3 h at room temperature. Then, the ligand L^{2Ad} (0.500 mmol, 0.191 g) was added, and the reaction was stirred for 24 h at room temperature. The solution was filtered, and the solvent was evaporated at reduced pressure, obtaining a white solid, which was washed with diethyl ether (10 mL) and *n*-hexane (10 mL) and dried under reduced pressure to give the complex [Cu(L^{2Ad})(PPh_3)]PF_6 in 56% yield. Mp: 282−296 °C. Solubility: CH_3OH, THF, CH_2Cl_2, $CHCl_3$, CH_3CN, and DMSO. FT-IR (cm^{-1}): 3379w (N−H); 3076wbr, 3013w, 2909w, 2859 (C−H); 1671m (C═O); 1562w; 1532m, 1481w, 1455w, 1436m (C═C/C═N); 1360w, 1350w, 1337w, 1310w, 1250w, 1225w, 1098m, 1041w, 998w; 834vs (PF_6); 821s, 785m, 752m, 740m, 692m, 667w, 595w, 571m, 556s, 531s. ^1H NMR ($CDCl_3$, 293 K): δ 1.53−2.56 (m, 27H, CH_{ADM} and CH_3), 5.93 (s, 2H, 4−CH_{Pz}), 6.81 (s, 1H, α−CH), 7.41−7.58 (m, 15H, CH_{ar}), 7.60 (m, 1H, N*H*). $^{13}C\{^1H\}$-NMR ($CDCl_3$, 293 K): δ 10.9, 13.7 (CH_3); 29.3, 36.0, 40.2 (CH_{ADM}); 107.0 (4-CH_{pz}); 128.9, 129.0, 130.4, 132.2, 132.5, 132.8, 133.7, 133.8, 142.7 (CH_{ar} and 5-CH_{pz}); 150.4 (3-CH_{pz}); 162.8 (*C*═O). $^{31}P\{^1H\}$-NMR ($CDCl_3$, 293 K): δ −144.02 (sept, J_{F-P} = 714 Hz), 7.49 (s). ESI-MS(+) (major positive ions, CH_3CN), *m*/*z* (%): 145 (30) $[Cu + 2CH_3CN]^+$, 366 (90) $[Cu(PPh_3) + CH_3CN]^+$, 485 (40) $[Cu(L^{2Ad}) + CH_3CN]^+$, 587 (40) $[Cu(PPh_3)_2]^+$, 706 (100) $[Cu(L^{2Ad})(PPh_3)]^+$. ESI-MS(−) (major negative ions, CH_3CN), *m*/*z* (%): 145 (100) $[PF_6]^-$. Elemental Analysis (%) calcd for $C_{40}H_{46}CuF_6N_5OP_2$: C 56.37, H 5.44, N 8.22; found: C 56.73, H 5.43, N 8.27.

4.2. X-ray Crystallography. A batch of several quite large blue crystals of complex **3**, suitable for X-ray investigations, was obtained by slow evaporation of an acetonitrile solution. A fragment of one of such crystals was chipped away from a larger specimen, picked up with a nylon loop, and mounted on the top of the goniometer head of a Rigaku-OD Gemini E diffractometer, equipped with a 2K × 2K EOS CCD area detector and sealed tube Enhance Cu/Mo X−ray sources. Raw X-ray diffraction data for complex **3** were obtained at room temperature [301(1) K] by means of the ω-scans technique using graphite-monochromated Cu Kα (λ = 1.54184) radiation in a 1024 × 1024 pixel mode and 2 × 2-pixel binning. Data collection, data reduction, finalization, and cell refinement were carried out using the CrysAlisPro software, Version 1.171.42.49 (Rigaku OD, 2022).[102] Diffraction intensities were corrected for absorption as well as for Lorentz and polarization effects. The absorption correction was performed by means of an empirical multiscan approach, with the scaling algorithm *SCALE3 ABSPACK*, using equivalent reflections. Accurate unit cell parameters were obtained by least-squares refinement of the angular settings of the 30056 strongest reflections, chosen throughout the whole data collection. Crystal stability was checked by monitoring two reference frames every 50 frames, and no significant change in peak intensities was observed; a manual data reduction was performed to account for sample wobbling. The structures were solved by direct phasing and refined by full-matrix

https://doi.org/10.1021/acs.jmedchem.4c00821
J. Med. Chem. XXXX, XXX, XXX−XXX

least-squares based on F_0^2 with the SHELXT[103] and SHELXL[104] programs through the Olex2 1.5 graphical interface.[105] All non-H atoms (except bromine; see below) were refined anisotropically. The positions of H atoms were calculated and refined with a riding model, with displacement parameters 1.2/1.5 times the U_{eq} of the parent atoms. In the unit cell, each molecule of the cationic complex **3** is accompanied by two bromide counteranions as well as by four water and two acetonitrile molecules whose occupation is crystallographically fixed at 0.5. The refinement of the complex cation did not prove difficult; the refinement of the positions of the bromide ions was instead challenging and demanded several attempts to model, as reported in the discussion. In the finally chosen scheme, in particular, each Br^- anion is disordered over four positions, whose site occupation factors were constrained to sum to 0.5 by applying a SUMP restraint (refined sofs of 0.17, 0.14, 0.13, and 0.06, respectively). All attempts to introduce anisotropy in the refinement of bromide ions (also applying restraints) led to unsatisfactory results, so these positions were refined only isotropically. Other RIGU restraints were applied to the CH_3CN molecule and C9, C10, C12, and C14 atoms of the amantadine ring. The hydrogen atoms bound to O2 (close to the position of disordered bromide) proved also to be troublesome. All attempts to introduce these atoms into the model invariably led to nonconvergency of the refinement procedure. For this reason, they were omitted from the final model. Full listings of atomic coordinates, bond lengths/angles, and anisotropic thermal parameters are available as Supporting Information, in the form of a .cif file. The crystallographic data have been deposited at the Cambridge Crystallographic Data Centre (CCDC), with a deposition number 2332100. The data can be obtained free of charge from The Cambridge Crystallographic Data Centre via www.ccdc.cam.ac.uk/structures.

4.3. Spectroscopic Methods. *4.3.1. Synchrotron Radiation-Induced X-ray Photoelectron Spectroscopy (XPS).* XPS measurements were carried out on the five coordination compounds deposited as thick films onto Au/Si(111) wafer substrates by following a drop-casting procedure. SR-XPS experiments were performed at the SuperESCA beamline at the ELETTRA synchrotron facility of Trieste (Italy), collecting the data in fixed analyzer transmission mode (pass energy = 5−20 eV), with the monochromator entrance and exit slits optimized at 30 and 20 μm, respectively. For the C 1s, O 1s, and N 1s spectral regions, a photon energy of 650 eV was used; for the C 1s, Au 4f, Cl 2p, and Br 3d spectral regions, a photon energy of 360 eV was used. For C 1s and Cu 2p spectral regions, a photon energy of 1100 eV was used. The energy resolution was ΔE = 0.25 eV. Calibration of the energy scale was made referencing the spectra to the C 1s core level signal of aliphatic carbons, found at 285.0 eV, for all samples.[106] Curve-fitting analysis of the C 1s, O 1s, N 1s, Au 4f (substrate reference), Cl 2p, Br 3d, and Cu 2p spectra was done using Gaussian curves as fitting functions, after subtraction of a polynomial background. The Cl $2p_{3/2,1/2}$ and Cu $2p_{3/2,1/2}$ doublets were fitted using the same full width at half-maximum (fwhm) for both components, a spin−orbit splitting of 1.6 and 19.8 eV, respectively, and a branching ratio ($2p_{3/2}/2p_{1/2}$) of 2. For the Br $3d_{5/2,3/2}$ doublets, a splitting of 6.6 eV, a branch ratio of $3d_{5/2}/3d_{3/2}$ of 3/2, and the same fwhm values for both spin−orbit components were applied. For the Au $4f_{7/2,5/2}$ doublets, a splitting of 3.7 eV, a branching ratio $4f_{7/2}/4f_{5/2}$ of 4/3, and the same fwhm values for both spin−orbit components were applied. When several different species were identified in a spectrum, the same fwhm value was set for all individual photoemission bands.

4.3.2. Near Edge X-ray Absorption Fine Structure (NEXAFS) Spectroscopy. NEXAFS experiments were performed at the BEAR beamline (Bending magnet for Emission Absorption and Reflectivity) at the ELETTRA storage ring, installed at the left exit of the 8.1 bending magnet exit. The apparatus is based on a bending magnet as a source and beamline optics delivering photons from 5 eV up to about 1600 eV with a selectable degree of ellipticity. The UHV end station is equipped with a movable hemispherical electron analyzer and a set of photodiodes to collect angle-resolved photoemission spectra, optical reflectivity, and fluorescence yield. In these experiments, we used ammeters to measure the drain current from the sample.

Investigations were carried out on thick films deposited onto Au/Si(111) substrates (same samples used to collect XPS spectra); C and N K-edge spectra were collected at grazing (20°) incidence angles of the linearly polarized photon beam with respect to the sample surface in order to maximize the signal intensity. The raw spectra were normalized to the incident photon flux by dividing the sample spectrum by the spectrum collected on a freshly sputtered gold surface; subsequently, a straight line that fits the part of the spectrum below the edge was subtracted from the value at 330.00 and 420.00 eV for C and N, respectively, was assessed to 1.

For the C K edge spectra, the energy scale was referenced to the $\pi^*_{C=O}$ transition of the amide function in the side chain of the L^{2Ad} ligand,[67] for the N K edge spectra to the π^*_2 transition of the pyrazole rings.[66]

4.3.3. X-ray Absorption Spectroscopy (XAS). XAS experiments were carried out at LISA (BM08) beamline[74] at the ESRF (European Synchrotron Radiation Facility) in Grenoble. The beamline is equipped with a Si(111) double crystal monochromator, a collimating, and a focusing mirror (before and after, respectively), both mirrors are also coated with Si (or Pt stripes), useful for harmonics rejection. The Cu complexes powders were dried in a vacuum, weighted and mixed with a suitable amount of cellulose (50−60 mg), and pressed into homogeneous pellets prior to the measurements. Cu K edge (8979 eV) was probed at ambient pressure and temperature in fluorescence geometry, using a 13-element HPGe ORTEC detector, while measuring the incident light using a $N_{2(g)}$-filled ionization chamber prior to the sample (I_0). During spectra acquisition, transmission geometry measurements were also collected using a secondary ionization chamber (I_1) right after the sample; this allowed one to compare the acquired spectra and verify the quality of the data (absence of self-absorption/Bragg peaks/edge deformations). Lastly, a metallic Cu foil was used as reference material for energy calibration, it was placed in between two $N_{2(g)}$-filled ionization chambers, (I_1 and I_2, right after the foil). Six to 8 scans were acquired and averaged for each sample and XAS signals from fluorescence, transmission, and reference foil, respectively, were calculated as follows:

$$\alpha_{fluo} = \frac{\sum I_{f_i}}{I_0}\alpha_{trasm} = \ln\left(\frac{I_0}{I_1}\right)\alpha_{ref} = \ln\left(\frac{I_1}{I_2}\right)$$

with $\sum I_f$ being the sum over the fluorescence signals of the elements of the detector obtained selecting the Cu K_α emission line from the total fluorescence yield.

Experimental spectra were treated along the standard procedures for background subtraction ($\alpha' = \alpha_{exp} - \alpha_{pre}$), edge jump normalization, and bare atom background subtraction (α_b)[82] to extract the EXAFS structural signals $\chi_{exp}(k) = \frac{\alpha' - \alpha_b}{\alpha_b}$. The edge energy ($E_o$) defines the energy scale of the photoelectron wavenumber $k[Å^{-1}] = \hbar^{-1}\sqrt{2m_e(E - E_0)}$ (where m_e is the mass of the electron, E and E_o in eV), and it was selected as the first inflection point (first maximum of the first derivative) for all spectra.

4.4. Cytotoxicity Studies. *4.4.1. Cell Culture.* Human glioblastoma U87, T98 and U251 cells (European Collection of Cell Cultures, Salisbury, UK) were maintained in Eagle's minimum essential medium (EMEM) (Gibco) supplemented with heat-inactivated fetal bovine serum (FBS, 10% v/v), penicillin (100 IU/mL) and streptomycin (100 μg/mL), 2 mmol/L L-glutamine, nonessential amino acids (10% v/v), and sodium pyruvate (10% v/v). Murine microglial BV2 cells were maintained in Dulbecco's modified Eagle medium (DMEM) (Gibco, Rodano, Italy) supplemented with FBS (10% v/v), penicillin (100 IU/mL), streptomycin (100 μg/mL) and sodium pyruvate (10% v/v). All cell lines were grown at 37 °C in a humidified atmosphere of 5% CO_2.

4.4.2. Compounds. Cisplatin and TTM (Sigma-Aldrich, Milan, Italy) were dissolved in DMSO. $CuBr_2$ and $CuCl_2$ were dissolved in H_2O. Cu complexes and $[Cu(CH_3CN)_4]PF_6$ were dissolved in

https://doi.org/10.1021/acs.jmedchem.4c00821
J. Med. Chem. XXXX, XXX, XXX−XXX

DMSO to obtain 10 mM stock solutions and diluted in medium in the same day of the experiment to adjust the final concentration of DMSO so that it does not exceed 0.5% (v/v) in cell cultures.

4.4.3. Cell Treatment and Analysis of Viability. The cytotoxic activity of Cu complexes was measured in U87, T98, U251, and BV2 cells using the MTT assay. Glioma cells were seeded in 96-well plates at 3×10^3 cells/well, BV2 cells at 1.5×10^3 cells/well. Cu complexes (**1**−**5**), $CuBr_2$, $CuCl_2$, and $[Cu(CH_3CN)_4]PF_6$ at a range of concentrations (1−50 μM), cisplatin (1−50 μM) or TTM (1−50 μM) were added to the medium, and cells were incubated for 72 h. In combination with experiments with TTM, cells were treated with Cu complexes **3** and **5** and TTM at the specific IC_{25} dose for each cell line. In combination experiments with TMZ, cells were treated with TMZ (100−900 μM) in combination with compounds **3** or **5** at IC_{25} doses specific for each cell line. After this incubation, MTT (0.8 mg/mL) was added to each well and further incubated for 3 h at 37 °C. Then, the culture medium was removed, 100 μL of DMSO/well was added to solve the formazan crystals, and the absorbance at 540 nm was quantified in a plate reader (BioTek Instruments, Winooski, VT, USA). All experiments were repeated thrice.

4.4.4. Morphological Analysis. To observe the effects of Cu compounds based on morphological changes, glioma cells were seeded at 2.5×10^4 cells/mL in 6-well plates and incubated for 72 h with compounds **3** and **5** under normal growth conditions. After incubation, the cellular morphology was observed using an inverted phase-contrast microscope (Nikon, Japan) at 10× magnification.

4.4.5. Cell Uptake Assay. To determine Cu compound uptake, glioma cells were seeded in 96-well plates at 3×10^3 cells/well and incubated for 24 h with compounds **3** and **5** under normal growth conditions. After incubation, cells were gently rinsed with PBS containing 200 μM EDTA to remove extracellular Cu complexes, and 5 μM BioTracker Green Copper diluted in culture medium was added in each well and incubated at 37 °C, 5% CO_2 for 3 h. Given that nonspecific fluorescence may be observed from acidic organelles, 100 nM bafilomycin A1 was added to the medium 30 min before the addition of Green Copper to suppress acidification of lysosome and also to the Green Copper solution. After the staining, cells were washed with PBS and observed with a C2 Plus confocal microscope (Nikon Instruments) at 40× magnification.

4.4.6. Cell Cycle Assay. The DNA content was measured with flow cytometry (FACS Accuri C6, BD Bioscience, San Jose, CA, USA), and the distribution of U87, T98, and U251 cells during the cell cycle phase was evaluated. Cells (2.5×10^4/mL) were plated into 12-well plates and treated with the specified vehicle or drugs for 72 h. Thereafter, cells were harvested with trypsin, and the cell pellets were fixed in ice-cold 70% ethanol at 4 °C overnight. The fixed cells were treated with RNase (100 μg/mL) at 37 °C for 30 min and stained with propidium iodide (PI, 20 μg/mL) at 4 °C in the dark for 30 min before measurement. Data were analyzed using a BD Accuri C6 Plus flow cytometer and its software (BD Biosciences, Milan, Italy).

4.4.7. Cell Proliferation Assay. CellTraceTM Cell Proliferation kit (Thermo Fisher Scientific, Rome, Italy) was used to analyze the proliferation of glioma cells in response to stimulation by compounds **3** and **5**. Cells were labeled with 1−2 μM carboxyfluorescein diacetate succinimidyl ester (CFSE) for 20 min at 37 °C, then seeded 2.5×10^4 cells/mL and cultured for 72 h in a culture medium containing compounds **3**, **5**, or vehicle. At the end of the treatment, florescence was analyzed by FACS.

4.4.8. Colony Formation Assay. Glioma cells were seeded in 6-well plates (500 cells/well) overnight, and then the medium was replaced with compounds **3** and **5** and changed every 3 days. After 2 weeks, 4% paraformaldehyde was added for 15 min for cell fixation, then washed with PBS and stained with 0.1% crystal violet for 15 min. The stained colonies were counted under the microscope and compared with the control samples. The colony area percentage was calculated on thresholded and intensity inverted regions that were single well images by ImageJ software (Version 1.54h).

4.4.9. Intracellular ROS Measurements. Intracellular ROS generation was measured in vitro using 5-(and-6)-carboxy-2′,7′-dichlorofluorescein diacetate (DCFDA). Cells (2.5×10^4 cells/mL) were seeded in a 12-well plate and the Cu complexes **3** and **5** or vehicle were added to the medium. In combination experiments, cells were treated with 600 μM TMZ in combination with compound **3** or **5** at IC_{25} doses specific for each cell line. Cells were incubated for 48−72 h. Cells were washed with PBS, pulsed with DCFDA for 10 min at 37 °C, 5% CO_2, and analyzed by a BD Accuri C6 Plus flow cytometer and its software.

4.4.10. γH2AX Measurement by a Flow Cytometer. Cells (2.5×10^4 cells/mL) were seeded in a 12-well plate and the Cu complexes **3** and **5** or vehicle were added to the medium. Cells were incubated for 72 h. Cells, fixed in 4% paraformaldehyde and permeabilized with T-PBS (PBS with 0.1% Tween-20) were incubated with anti-γH2AX antibody (1:200, Cell Signaling, Pero, Italy) in T-PBST containing 1% BSA for 1 h at room temperature. Cells were then incubated with an Alexa Fluor 647-labeled antirabbit antibody (Abcam, Cambridge, UK) and analyzed by a flow cytometer.

4.4.11. Statistical Analysis. GraphPad Prism 9.0.1(128) software (GraphPad Software, San Diego, CA, USA) was used for statistical analysis. The results represent the mean ± standard error of the mean (SEM) of three experiments. One-way analysis of variance (ANOVA) followed by Tukey's multiple comparison test. The statistical significance in the cell-cycle distributions was determined using the chi-square test. $p < 0.05$ values were considered to be statistically significant ($^*p < 0.05$, $^{**}p < 0.01$, $^{***}p < 0.001$, $^{****}p < 0.0001$).

■ ASSOCIATED CONTENT

Data Availability Statement

CCDC 2332100 contains the supplementary crystallographic data for this paper. The data can be obtained free of charge from the Cambridge Crystallographic Data Centre via www.ccdc.cam.ac.uk/structures.

Supporting Information

The Supporting Information is available free of charge at https://pubs.acs.org/doi/10.1021/acs.jmedchem.4c00821.

Molecular formula strings (CSV)

Extended version of the structural commentary for complex **3**; other figures and tables (PDF)

■ AUTHOR INFORMATION

Corresponding Authors

Fabio Del Bello − *School of Pharmacy, Medicinal Chemistry Unit, University of Camerino, 62032 Camerino, Italy;* orcid.org/0000-0001-6538-6029; Phone: +390737402265; Email: fabio.delbello@unicam.it

Chiara Battocchio − *Department of Science, Roma Tre University, 00146 Roma, Italy;* orcid.org/0000-0003-4590-0865; Phone: +390657333400; Email: chiara.battocchio@uniroma3.it

Authors

Maria Beatrice Morelli − *School of Pharmacy, Immunopathology and Molecular Medicine Unit, University of Camerino, 62032 Camerino, Italy*

Miriam Caviglia − *School of Science and Technology, Chemistry Division, University of Camerino, 62032 Camerino, Italy*

Carlo Santini − *School of Science and Technology, Chemistry Division, University of Camerino, 62032 Camerino, Italy;* orcid.org/0000-0002-3942-1713

Jo' Del Gobbo − *School of Science and Technology, Chemistry Division, University of Camerino, 62032 Camerino, Italy;* orcid.org/0009-0002-8969-0900

Laura Zeppa − *School of Pharmacy, Immunopathology and Molecular Medicine Unit, University of Camerino, 62032 Camerino, Italy*

https://doi.org/10.1021/acs.jmedchem.4c00821
J. Med. Chem. XXXX, XXX, XXX−XXX

Gianfabio Giorgioni − *School of Pharmacy, Medicinal Chemistry Unit, University of Camerino, 62032 Camerino, Italy;* orcid.org/0000-0002-9576-6580
Alessandro Piergentili − *School of Pharmacy, Medicinal Chemistry Unit, University of Camerino, 62032 Camerino, Italy;* orcid.org/0000-0001-6135-6826
Wilma Quaglia − *School of Pharmacy, Medicinal Chemistry Unit, University of Camerino, 62032 Camerino, Italy;* orcid.org/0000-0002-7708-0200
Federica Bertelà − *Department of Science, Roma Tre University, 00146 Roma, Italy*
Simone Amatori − *Department of Science, Roma Tre University, 00146 Roma, Italy*
Carlo Meneghini − *Department of Science, Roma Tre University, 00146 Roma, Italy;* orcid.org/0000-0003-4846-8422
Giovanna Iucci − *Department of Science, Roma Tre University, 00146 Roma, Italy;* orcid.org/0000-0002-6478-3759
Iole Venditti − *Department of Science, Roma Tre University, 00146 Roma, Italy;* orcid.org/0000-0002-9306-573X
Alessandro Dolmella − *Department of Pharmaceutical and Pharmacological Sciences, University of Padova, 35131 Padova, Italy*
Michele Di Palma − *Department of Biomedical Sciences, University of Padova, 35131 Padova, Italy*
Maura Pellei − *School of Science and Technology, Chemistry Division, University of Camerino, 62032 Camerino, Italy;* orcid.org/0000-0001-5020-1730

Complete contact information is available at: https://pubs.acs.org/10.1021/acs.jmedchem.4c00821

Funding

This research was funded by Unione Europea−NextGenerationEU (MUR-Fondo Promozione e Sviluppo - D.M. 737/2021, INVIRCuM and PROCARAPINE, University of Camerino, FAR 2022 PNR, and NGEU PNRR, D.M. n. 351/2022 M4C1 I4.1) and by the University of Padova (PRID BIRD225980).

Notes

The authors declare no competing financial interest.

■ ACKNOWLEDGMENTS

Authors from Roma Tre University gratefully acknowledge the European Synchrotron Radiation Facility for the provision of synchrotron radiation facilities (ESRF proposal ih-mh58) and thank Dr. Francesco D'Acapito, Dr. Jacopo Orsilli, and Dr. Alessandro Puri for assistance in using beamline BM08 (LISA). In addition, the authors of Roma Tre acknowledge the CERIC−ERIC Consortium for access to experimental facilities (LISA − ESRF; SUES − Elettra) and financial support (proposal #20232011). The Grant of Excellence Departments MIUR (ARTICOLO 1, COMMI 314−337 LEGGE 232/2016) is also gratefully acknowledged by the authors of Roma Tre.

■ ABBREVIATIONS USED

CCDC, Cambridge crystallographic data centre; CFSE, carboxyfluorescein diacetate succinimidyl ester; DFT, density functional theory; DIPEA, diisopropylethylamine; DMEM, Dulbecco's modified Eagle medium; DNA, desossiribonucleic acid; DSBs, DNA double-strand breaks; EMEM, Eagle's minimum essential medium; ESRF, european synchrotron radiation facility; GBM, glioblastoma; GSH, glutathione; HSQC, heteronuclear single quantum coherence; MTT, 3-[4,5-dime-thylthiazole-2-yl]-2,5-dimethyltetrazolium bromide; NEXAFS, near edge X-ray absorption fine structure; PPh_3, triphenylphosphine; PTA, 1,3,5-triaza-7-phosphaadamantane; ROS, reactive oxygen species; SR-XPS, synchrotron radiation-induced X-ray photoelectron spectroscopy; TBTU, 2-(1H-benzotriazole-1-yl)-1,1,3,3-tetramethylaminium tetrafluoroborate; TMZ, temozolomide; TTM, tetrathiomolybdate; XAS, X-ray absorption spectroscopy; XPS, X-ray photoelectron spectroscopy.

■ REFERENCES

(1) Allardyce, C. S.; Dyson, P. J. Metal-based drugs that break the rules. *Dalton Trans.* **2016**, *45* (8), 3201−3209.
(2) Spreckelmeyer, S.; Orvig, C.; Casini, A. Cellular Transport Mechanisms of Cytotoxic Metallodrugs: An Overview beyond Cisplatin. *Molecules* **2014**, *19* (10), 15584−15610.
(3) Chen, S. H.; Chang, J. Y. New Insights into Mechanisms of Cisplatin Resistance: From Tumor Cell to Microenvironment. *Int. J. Mol. Sci.* **2019**, *20* (17), 4136.
(4) Oun, R.; Moussa, Y. E.; Wheate, N. J. The side effects of platinum-based chemotherapy drugs: a review for chemists. *Dalton Trans.* **2018**, *47* (19), 6645−6653.
(5) Florea, A.-M.; Büsselberg, D. Cisplatin as an Anti-Tumor Drug: Cellular Mechanisms of Activity, Drug Resistance and Induced Side Effects. *Cancers* **2011**, *3* (1), 1351−1371.
(6) Lelievre, P.; Sancey, L.; Coll, J. L.; Deniaud, A.; Busser, B. The Multifaceted Roles of Copper in Cancer: A Trace Metal Element with Dysregulated Metabolism, but Also a Target or a Bullet for Therapy. *Cancers* **2020**, *12* (12), 3594.
(7) Molinaro, C.; Martoriati, A.; Pelinski, L.; Cailliau, K. Copper Complexes as Anticancer Agents Targeting Topoisomerases I and II. *Cancers* **2020**, *12* (10), 2863.
(8) Zaki, M.; Arjmand, F.; Tabassum, S. Current and future potential of metallo drugs: Revisiting DNA-binding of metal containing molecules and their diverse mechanism of action. *Inorg. Chim. Acta* **2016**, *444* (Supplement C), 1−22.
(9) Santini, C.; Pellei, M.; Gandin, V.; Porchia, M.; Tisato, F.; Marzano, C. Advances in Copper Complexes as Anticancer Agents. *Chem. Rev.* **2014**, *114* (1), 815−862.
(10) Medici, S.; Peana, M.; Nurchi, V. M.; Lachowicz, J. I.; Crisponi, G.; Zoroddu, M. A. Noble metals in medicine: Latest advances. *Coord. Chem. Rev.* **2015**, *284* (Supplement C), 329−350.
(11) Zhang, K.; Qu, C.; Zhou, P.; Yang, Z.; Wu, X. Integrative analysis of the cuproptosis-related gene ATP7B in the prognosis and immune infiltration of IDH1 wild-type glioma. *Gene* **2024**, *905*, No. 148220.
(12) Xie, J. M.; Yang, Y. N.; Gao, Y. B.; He, J. Cuproptosis: mechanisms and links with cancers. *Mol. Cancer* **2023**, *22* (1), 46.
(13) Ikram, M.; Rehman, S.; Feroz, I.; Khan, R.; Sinnokrot, M. O.; Subhan, F.; Naeem, M.; Schulzke, C.; Schulzke, C. Synthesis, spectral, Hirshfeld surface analysis and biological evaluation of a Schiff base copper(II) complex: Towards a copper(II) based human anti-glioblastoma agent. *J. Mol. Struct.* **2023**, *1278*, No. 134960.
(14) Castillo-Rodríguez, R. A.; Palencia, G.; Anaya-Rubio, I.; Gallardo-Pérez, J. C.; Jiménez-Farfán, D.; Escamilla-Ramírez, A.; Zavala-Vega, S.; Cruz-Salgado, A.; Cervantes-Rebolledo, C.; Gracia-Mora, I.; Ruiz-Azuara, L.; Trejo-Solis, C. Anti-proliferative, pro-apoptotic and anti-invasive effect of the copper coordination compound Cas III-La through the induction of reactive oxygen species and regulation of Wnt/β-catenin pathway in glioma. *J. Cancer* **2021**, *12* (19), 5693−5711.
(15) Shimada, K.; Reznik, E.; Stokes, M. E.; Krishnamoorthy, L.; Bos, P. H.; Song, Y. Y.; Quartararo, C. E.; Pagano, N. C.; Carpizo, D. R.; Decarvalho, A. C.; Lo, D. C.; Stockwell, B. R. Copper-Binding Small Molecule Induces Oxidative Stress and Cell-Cycle Arrest in

Glioblastoma-Patient-Derived Cells. *Cell Chem. Biol.* **2018**, *25* (5), 585−594.
(16) Buccarelli, M.; D'Alessandris, Q. G.; Matarrese, P.; Mollinari, C.; Signore, M.; Cappannini, A.; Martini, M.; D'Aliberti, P.; De Luca, G.; Pedini, F.; Boe, A.; Biffoni, M.; Pallini, R.; Ricci-Vitiani, L. Elesclomol-induced increase of mitochondrial reactive oxygen species impairs glioblastoma stem-like cell survival and tumor growth. *J. Exp. Clin. Cancer Res.* **2021**, *40* (1), 228.
(17) Tan, A. C.; Ashley, D. M.; López, G. Y.; Malinzak, M.; Friedman, H. S.; Khasraw, M. Management of glioblastoma: State of the art and future directions. *Ca-Cancer J. Clin.* **2020**, *70* (4), 299−312.
(18) Li, X.; Shao, F. L.; Sun, J.; Du, K.; Sun, Y.; Feng, F. D. Enhanced Copper-Temozolomide Interactions by Protein for Chemotherapy against Glioblastoma Multiforme. *ACS Appl. Mater. Interfaces* **2019**, *11* (45), 41935−41945.
(19) Verdugo, E.; Puerto, I.; Medina, M. A. An update on the molecular biology of glioblastoma, with clinical implications and progress in its treatment. *Cancer Communications* **2022**, *42* (11), 1083−1111.
(20) Eisenbarth, D.; Wang, Y. A. Glioblastoma heterogeneity at single cell resolution. *Oncogene* **2023**, *42* (27), 2155−2165.
(21) Gandin, V.; Ceresa, C.; Esposito, G.; Indraccolo, S.; Porchia, M.; Tisato, F.; Santini, C.; Pellei, M.; Marzano, C. Therapeutic potential of the phosphino Cu(I) complex (HydroCuP) in the treatment of solid tumors. *Sci. Rep.* **2017**, *7* (1), No. 13936.
(22) Marinelli, M.; Santini, C.; Pellei, M. Recent Advances in Medicinal Applications of Coinage-Metal (Cu and Ag) N-Heterocyclic Carbene Complexes. *Curr. Top. Med. Chem.* **2016**, *16* (26), 2995−3017.
(23) Gandin, V.; Tisato, F.; Dolmella, A.; Pellei, M.; Santini, C.; Giorgetti, M.; Marzano, C.; Porchia, M. In Vitro and in Vivo Anticancer Activity of Copper(I) Complexes with Homoscorpionate Tridentate Tris(pyrazolyl)borate and Auxiliary Monodentate Phosphine Ligands. *J. Med. Chem.* **2014**, *57* (11), 4745−4760.
(24) Pellei, M.; Gioia Lobbia, G.; Papini, G.; Santini, C. Synthesis and properties of poly(pyrazolyl)borate and related boron-centered scorpionate ligands. Part B: imidazole-, triazole- and other heterocycle-based systems. *Mini-Rev. Org. Chem.* **2010**, *7*, 173−203.
(25) Marzano, C.; Pellei, M.; Colavito, D.; Alidori, S.; Gioia Lobbia, G.; Gandin, V.; Tisato, F.; Santini, C. Synthesis, characterization, and in vitro antitumor properties of tris(hydroxymethyl)phosphine copper(I) complexes containing the new bis(1,2,4-triazol-1-yl)acetate ligand. *J. Med. Chem.* **2006**, *49* (25), 7317−7324.
(26) Santini, C.; Pellei, M.; Gioia Lobbia, G.; Fedeli, D.; Falcioni, G. Synthesis and characterization of new copper(I) complexes containing 4-(diphenylphosphane)benzoic acid and "scorpionate" ligands with "in vitro" superoxide scavenging activity. *J. Inorg. Biochem.* **2003**, *94* (4), 348−354.
(27) Santini, C.; Pellei, M.; Gioia Lobbia, G.; Cingolani, A.; Spagna, R.; Camalli, M. Unprecedented phosphino copper(I) derivatives of tris(pyrazolyl)methanesulfonate ligand co-ordinated to metal in an unusual κ3-N, N′ O fashion. *Inorg. Chem. Commun.* **2002**, *5* (6), 430−433.
(28) Del Bello, F.; Pellei, M.; Bagnarelli, L.; Santini, C.; Giorgioni, G.; Piergentili, A.; Quaglia, W.; Battocchio, C.; Iucci, G.; Schiesaro, I.; Meneghini, C.; Venditti, I.; Ramanan, N.; De Franco, M.; Sgarbossa, P.; Marzano, C.; Gandin, V. Cu(I) and Cu(II) Complexes Based on Lonidamine-Conjugated Ligands Designed to Promote Synergistic Antitumor Effects. *Inorg. Chem.* **2022**, *61* (12), 4919−4937.
(29) Pellei, M.; Bagnarelli, L.; Luciani, L.; Del Bello, F.; Giorgioni, G.; Piergentili, A.; Quaglia, W.; De Franco, M.; Gandin, V.; Marzano, C.; Santini, C. Synthesis and Cytotoxic Activity Evaluation of New Cu(I) Complexes of Bis(pyrazol-1-yl) Acetate Ligands Functionalized with an NMDA Receptor Antagonist. *Int. J. Mol. Sci.* **2020**, *21* (7), 2616.
(30) Pellei, M.; Gandin, V.; Cimarelli, C.; Quaglia, W.; Mosca, N.; Bagnarelli, L.; Marzano, C.; Santini, C. Syntheses and biological studies of nitroimidazole conjugated heteroscorpionate ligands and related Cu(I) and Cu(II) complexes. *J. Inorg. Biochem.* **2018**, *187*, 33−40.
(31) Morelli, M. B.; Amantini, C.; Santoni, G.; Pellei, M.; Santini, C.; Cimarelli, C.; Marcantoni, E.; Petrini, M.; Del Bello, F.; Giorgioni, G.; Piergentili, A.; Quaglia, W. Novel antitumor copper(ii) complexes designed to act through synergistic mechanisms of action, due to the presence of an NMDA receptor ligand and copper in the same chemical entity. *New J. Chem.* **2018**, *42* (14), 11878−11887.
(32) Krasowska, D.; Gerkowicz, A.; Wróblewska-Luczka, P.; Grabarska, A.; Zaluska-Ogryzek, K.; Krasowska, D.; Luszczki, J. J. Anticancer Activity of Amantadine and Evaluation of Its Interactions with Selected Cytostatics in Relation to Human Melanoma Cells. *Int. J. Mol. Sci.* **2022**, *23* (14), 7653.
(33) Kasemsuk, T.; Kaeopu, R.; Yubolphan, R.; Phuagkhaopong, S.; Vivithanaporn, P. Apoptotic and antiproliferative effects of amantadine and rimantadine in glioblastoma cells. *Thai J. Pharm. Sci.* **2019**, *43* (3), 119−124.
(34) Lan, Z. M.; Chong, Z. Y.; Liu, C.; Feng, D. Y.; Fang, D. H.; Zang, W. J.; Zhou, J. Amantadine inhibits cellular proliferation and induces the apoptosis of hepatocellular cancer cells *in vitro*. *Int. J. Mol. Sci.* **2015**, *36* (3), 904−910.
(35) Wanka, L.; Iqbal, K.; Schreiner, P. R. The Lipophilic Bullet Hits the Targets: Medicinal Chemistry of Adamantane Derivatives. *Chem. Rev.* **2013**, *113* (5), 3516−3604.
(36) Shehadi, I. A.; Delmani, F. A.; Jaber, A. M.; Hammad, H.; AlDamen, M. A.; Al-Qawasmeh, R. A.; Khanfar, M. A. Synthesis, Characterization and Biological Evaluation of Metal Adamantyl 2-Pyridylhydrazone Complexes. *Molecules* **2020**, *25* (11), 2530.
(37) Nakamoto, K., Applications in Coordination Chemistry. In *Infrared and Raman Spectra of Inorganic and Coordination Compounds*, 2008; Chapter 1, 1−273.
(38) Corazza, A.; Harvey, I.; Sadler, P. J. H-1,C-13-NMR and X-ray absorption studies of copper(I) glutathione complexes. *Eur. J. Biochem.* **1996**, *236* (2), 697−705.
(39) Xiao, Z. G.; Brose, J.; Schimo, S.; Ackland, S. M.; La Fontaine, S.; Wedd, A. G. Unification of the Copper(I) Binding Affinities of the Metallo-chaperones Atx1, Atox1, and Related Proteins DETECTION PROBES AND AFFINITY STANDARDS. *J. Biol. Chem.* **2011**, *286* (13), 11047−11055.
(40) Gaona, M. A.; de la Cruz-Martínez, F.; Caballero, M. P.; Francés-Poveda, E.; Rodríguez, A. M.; Rodríguez-Diéguez, A.; North, M.; Castro-Osma, J. A.; Lara-Sánchez, A. Closing the loop in the synthesis of heteroscorpionate-based aluminium helicates: catalytic studies for cyclic carbonate synthesis. *Dalton Trans.* **2022**, *51* (30), 11302−11315.
(41) Davies-Brooks, C., *New and Improved CSD − The 2023 November Data Update. Cambridge Structural Database (CSD)*: 2023. https://www.ccdc.cam.ac.uk/discover/blog/new-and-improved-csd-the-2023-november-data-update/.
(42) Allen, F. The Cambridge Structural Database: a quarter of a million crystal structures and rising. *Acta Crystallogr., Sect. B: Struct. Sci.* **2002**, *58* (3 Part 1), 380−388.
(43) Quillian, B.; Lynch, W. E.; Padgett, C. W.; Lorbecki, A.; Petrillo, A.; Tran, M. Syntheses and Crystal Structures of Copper(II) Bis(pyrazolyl)acetic Acid Complexes. *J. of Chemical Crystallography* **2019**, *49* (1), 1−7.
(44) Kozlevcar, B.; Pockaj, M.; Kitanovski, N. IR analysis of the carboxylate forms in structurally determined CuII(κ3-L)2 species isolated from different acidic solutions. *Maced. J. Chem. Chem. Eng.* **2015**, *34* (1), 133−138.
(45) Bhattacharyya, S.; Sarkar, A.; Dey, S. K.; Jose, G. P.; Mukherjee, A.; Sengupta, T. K. Copper(II) complex of methionine conjugated bis-pyrazole based ligand promotes dual pathway for DNA cleavage. *Dalton Trans.* **2013**, *42* (32), 11709−11719.
(46) Kozlevcar, B.; Gamez, P.; de Gelder, R.; Jaglicic, Z.; Strauch, P.; Kitanovski, N.; Reedijk, J. Counterion and Solvent Effects on the Primary Coordination Sphere of Copper(II) Bis(3,5-dimethylpyrazol-1-yl)acetic Acid Coordination Compounds. *Eur. J. Inorg. Chem.* **2011**, *24*, 3650−3655.

https://doi.org/10.1021/acs.jmedchem.4c00821
J. Med. Chem. XXXX, XXX, XXX−XXX

(47) Türkoglu, G.; Heinemann, F. W.; Burzlaff, N. Transition metal complexes bearing a 2,2-bis(3,5-dimethylpyrazol-1-yl)propionate ligand: one methyl more matters. *Dalton Trans.* **2011**, *40* (17), 4678−4686.
(48) Türkoglu, G.; Ulldemolins, C. P.; Müller, R.; Hübner, E.; Heinemann, F. W.; Wolf, M.; Burzlaff, N. Bis(3,5-dimethyl-4-vinylpyrazol-1-yl)acetic Acid: A New Heteroscorpionate Building Block for Copolymers that Mimic the 2-His-1-carboxylate Facial Triad. *Eur. J. Inorg. Chem.* **2010**, *19*, 2962−2974.
(49) Chandrasekhar, V.; Thilagar, P.; Senapati, T. Transition metal-assisted hydrolysis of pyrazole-appended organooxotin carboxylates accompanied by ligand transfer. *Eur. J. Inorg. Chem.* **2007**, *7*, 1004−1009.
(50) Kozlevčar, B.; Gamez, P.; de Gelder, R.; Driessen, W. L.; Reedijk, J. Unprecedented Change of the Jahn−Teller Axis in a Centrosymmetric CuII Complex Induced by Lattice Water Molecules−Crystal and Molecular Structures of Bis[bis(3,5-dimethylpyrazol-1-yl)acetato]copper(II) and Its Dihydrate. *Eur. J. Inorg. Chem.* **2003**, *2003* (1), 47−50.
(51) Honrado, M.; Sobrino, S.; Fernández-Baeza, J.; Sánchez-Barba, L. F.; Garcés, A.; Lara-Sánchez, A.; Rodríguez, A. M. Synthesis of an enantiopure scorpionate ligand by a nucleophilic addition to a ketenimine and a zinc initiator for the isoselective ROP of *rac*-lactide. *Chem. Commun.* **2019**, *55* (61), 8947−8950.
(52) Coulton, J. B.; Smith, A. C.; Wheeler, K. A.; Semeniuc, R. F. Multiple coordination modes of a new ditopic bis(pyrazolyl)methane-based ligand. *Dalton Transactions* **2018**, *47* (47), 17109−17121.
(53) Castro-Osma, J. A.; Alonso-Moreno, C.; Lara-Sánchez, A.; Otero, A.; Fernández-Baeza, J.; Sánchez-Barba, L. F.; Rodríguez, A. M. Catalytic behaviour in the ring-opening polymerisation of organo-aluminiums supported by bulky heteroscorpionate ligands. *Dalton Trans.* **2015**, *44*, 12388−12400.
(54) Roa, A. E.; Campos, J.; Paneque, M.; Salazar, V.; Otero, A.; Lara-Sanchez, A.; Rodriguez, A. M.; Lopez-Solera, I.; Gomez, M. V. Synthesis of new heteroscorpionate iridium(i) and iridium(iii) complexes. *Dalton Trans.* **2015**, *44*, 6987−6998.
(55) Bhattacharyya, S.; Sarkar, A.; Dey, S. K.; Mukherjee, A. Effect of glucosamine conjugation to zinc(II) complexes of a bis-pyrazole ligand: Syntheses, characterization and anticancer activity. *J. Inorg. Biochem.* **2014**, *140*, 131−142.
(56) Sun, J. P.; Zhao, D. W.; Song, H. B.; Tang, L. F. (Pyrazol-1-yl)carbonyl and Ester-Functionalized Bis(pyrazol-1-yl)methide Carbonyl Tungsten Complexes. *Organometallics* **2014**, *33* (17), 4425−4432.
(57) Jones, M. W.; Baldwin, J. E.; Cowley, A. R.; Dilworth, J. R.; Karpov, A.; Smiljanic, N.; Thompson, A. L.; Adlington, R. M. Synthesis of new bulky bis(pyrazolyl)methane carboxylate (heteroscorpionate) ligands and their complexes with iron, manganese and nickel. *Dalton Trans.* **2012**, *41* (46), 14068−14086.
(58) Pellei, M.; Papini, G.; Trasatti, A.; Giorgetti, M.; Tonelli, D.; Minicucci, M.; Marzano, C.; Gandin, V.; Aquilanti, G.; Dolmella, A.; Santini, C. Nitroimidazole and glucosamine conjugated heteroscorpionate ligands and related copper(II) complexes. Syntheses, biological activity and XAS studies. *Dalton Trans.* **2011**, *40* (38), 9877−9888.
(59) Otero, A.; Lara-Sanchez, A.; Fernandez-Baeza, J.; Martinez-Caballero, E.; Marquez-Segovia, I.; Alonso-Moreno, C.; Sanchez-Barba, L. F.; Rodriguez, A. M.; Lopez-Solera, I. New achiral and chiral NNE heteroscorpionate ligands. Synthesis of homoleptic lithium complexes as well as halide and alkyl scandium and yttrium complexes. *Dalton Trans.* **2010**, *39* (3), 930−940.
(60) Del Gobbo, J.; Santini, C.; Dolmella, A.; Li, Z.; Caviglia, M.; Pellei, M. New Copper Complexes with N,O-Donor Ligands Based on Pyrazole Moieties Supported by 3-Substituted Acetylacetone Scaffolds. *Molecules* **2024**, *29* (3), 621.
(61) Macrae, C. F.; Bruno, I. J.; Chisholm, J. A.; Edgington, P. R.; McCabe, P.; Pidcock, E.; Rodriguez-Monge, L.; Taylor, R.; van de Streek, J.; Wood, P. A. Mercury CSD 2.0 - new features for the visualization and investigation of crystal structures. *J. Appl. Crystallogr.* **2008**, *41* (2), 466−470.
(62) Drolet, D. P.; Manuta, D. M.; Lees, A. J.; Katnani, A. D.; Coyle, G. J. FT-IR and XPS study of copper(II) complexes of imidazole and benzimidazole. *Inorg. Chim. Acta* **1988**, *146* (2), 173−180.
(63) Folkesson, B.; Sundberg, P.; Johansson, L.; Larsson, R. An ESCA investigation of some copper complexes. *J. Electron Spectrosc. Relat. Phenom.* **1983**, *32* (3), 245−256.
(64) Lee, A. Y. *NIST Standard Reference Number 20*; National Institute of Standards and Technology: Gaithersburg MD, 20899, 2000. http://srdata.nist.gov/xps/=NIST (accessed 30/01/2024).
(65) Sesselmann, W.; Chuang, T. J. The interaction of chlorine with copper. 1. Adsorption and surface-reaction. *Surf. Sci.* **1986**, *176* (1−2), 32−66.
(66) Gabrielli, S.; Pellei, M.; Venditti, I.; Fratoddi, I.; Battocchio, C.; Iucci, G.; Schiesaro, I.; Meneghini, C.; Palmieri, A.; Marcantoni, E.; Bagnarelli, L.; Vallesi, R.; Santini, C. Development of new and efficient copper(II) complexes of hexyl bis(pyrazolyl)acetate ligands as catalysts for allylic oxidation. *Dalton Trans.* **2020**, *49* (44), 15622−15632.
(67) Stöhr, J. *NEXAFS Spectroscopy*; Springer-Verlag Berlin Heidelberg: Berlin Heidelberg GmbH, 1992; *25*.
(68) Mobilio, S.; Boscherini, F.; Meneghini, C. *Synchrotron Radiation. Basics, Methods and Applications*. 1 ed.; Springer-Verlag: Berlin Heidelberg, 2015; XXIV, 799.
(69) Lopez, A.; Amatori, S.; Olivieri, E.; Venditti, I.; Iucci, G.; Meneghini, C.; Bertelà, F.; Del Bello, F.; Quaglia, W.; Pellei, M.; Santini, C.; Battocchio, C. Cu(I) Coordination Compounds Conjugated to Au Nanorods for Future Applications in Drug Delivery: Insights in Molecular, Electronic and Cu Local Structure in Solid and Liquid Phase. *ChemPhysChem* **2024**, No. e202400074.
(70) Hanwell, M. D.; Curtis, D. E.; Lonie, D. C.; Vandermeersch, T.; Zurek, E.; Hutchison, G. R. Avogadro: an advanced semantic chemical editor, visualization, and analysis platform. *J. Cheminform.* **2012**, *4*, 17.
(71) Neese, F. Software update: The ORCA program system-Version 5.0. *WIREs: Comput. Mol. Sci.* **2022**, *12* (5), No. e1606.
(72) Neese, F. The ORCA program system. *Wiley Interdiscip. Rev.: Comput. Mol. Sci.* **2012**, *2* (1), 73−78.
(73) Ankudinov, A. L.; Ravel, B.; Rehr, J. J.; Conradson, S. D. Real-space multiple-scattering calculation and interpretation of x-ray-absorption near-edge structure. *Phys. Rev. B* **1998**, *58* (12), 7565−7576.
(74) D'Acapito, F.; Lepore, G. O.; Puri, A.; Laloni, A.; La Manna, F.; Dettona, E.; De Luisa, A.; Martin, A. The LISA beamline at ESRF. *J. Synchrotron Radiat.* **2019**, *26* (2), 551−558.
(75) Kau, L. S.; Spira-Solomon, D. J.; Penner-Hahn, J. E.; Hodgson, K. O.; Solomon, E. I. X-ray absorption edge determination of the oxidation state and coordination number of copper. Application to the type 3 site in Rhus vernicifera laccase and its reaction with oxygen. *J. Am. Chem. Soc.* **1987**, *109* (21), 6433−6442.
(76) Sano, M.; Komorita, S.; Yamatera, H. XANES spectra of copper(II) complexes - Correlation of the intensity of the 1s-3d transition and the shape of the complex. *Inorg. Chem.* **1992**, *31* (3), 459−463.
(77) Yamamoto, T. Assignment of pre-edge peaks in K-edge x-ray absorption spectra of 3d transition metal compounds: electric dipole or quadrupole? *X-Ray Spectrometry* **2008**, *37* (6), 572−584.
(78) Zhang, R. Q.; McEwen, J. S. Local Environment Sensitivity of the Cu K-Edge XANES Features in Cu-SSZ-13: Analysis from First-Principles. *J. Phys. Chem. Lett.* **2018**, *9* (11), 3035−3042.
(79) Bunker, G. *Introduction to XAFS: A Practical Guide to X-ray Absorption Fine Structure Spectroscopy*; Cambridge University Press: Cambridge, 2010.
(80) Rehr, J. J.; Albers, R. C. Theoretical approaches to X-ray absorption fine structure. *Rev. Mod. Phys.* **2000**, *72* (3), 621−654.
(81) Sayers, D. E.; Stern, E. A.; Lytle, F. W. New technique for investigating noncrystalline structures: Fourier analysis of the extended X-ray - absorption fine structure. *Phys. Rev. Lett.* **1971**, *27* (18), 1204−1207.

https://doi.org/10.1021/acs.jmedchem.4c00821
J. Med. Chem. XXXX, XXX, XXX−XXX

(82) Meneghini, C.; Bardelli, F.; Mobilio, S. ESTRA-FitEXA: A software package for EXAFS data analysis. *Nucl. Instrum. Methods Phys. Res., Sect. B* **2012**, *285*, 153−157.
(83) Tokar, E. J.; Boyd, W. A.; Freedman, J. H.; Waalkes, M. P., Toxic Effects of Metals. In *Casarett and Doull's Toxicology: The Basic Science of Poisons, 8e*, Klaassen, C. D., Ed.; McGraw-Hill Education: New York, NY, 2012.
(84) Jomova, K.; Valko, M. Advances in metal-induced oxidative stress and human disease. *Toxicology* **2011**, *283* (2−3), 65−87.
(85) Gaetke, L. M.; Chow, C. K. Copper toxicity, oxidative stress, and antioxidant nutrients. *Toxicology* **2003**, *189* (1−2), 147−163.
(86) Rossi, L.; Arciello, M.; Capo, C.; Rotilio, G. Copper imbalance and oxidative stress in neurodegeneration. *Ital. J. Biochem.* **2006**, *55* (3−4), 212−221.
(87) Lippard, S. J. Biochemistry - Free copper ions in the cell? *Science* **1999**, *284* (5415), 748−749.
(88) Halliwell, B.; Gutteridge, J. M. Oxygen toxicity, oxygen radicals, transition metals and disease. *Biochem. J.* **1984**, *219* (1), 1−14.
(89) Powell, S. R. The antioxidant properties of zinc. *J. Nutr.* **2000**, *130* (5), 1447S−1454S.
(90) Burkitt, M. J. A critical overview of the chemistry of copper-dependent low density lipoprotein oxidation:: Roles of lipid hydroperoxides, α-tocopherol, thiols, and ceruloplasmin. *Arch. Biochem. Biophys.* **2001**, *394* (1), 117−135.
(91) Chow, C. K. Vitamin E and oxidative stress. *Free Radic. Biol. Med.* **1991**, *11* (2), 215−232.
(92) Liang, Q.; Dedon, P. C. Cu(II)/H2O2-induced DNA damage is enhanced by packaging of DNA as a nucleosome. *Chem. Res. Toxicol.* **2001**, *14* (4), 416−422.
(93) Hayashi, M.; Kuge, T.; Endoh, D.; Nakayama, K.; Arikawa, J.; Takazawa, A.; Okui, T. Hepatic copper accumulation induces DNA strand breaks in the liver cells of Long-Evans Cinnamon strain rats. *Biochem. Biophys. Res. Commun.* **2000**, *276* (1), 174−178.
(94) Buettner, G. R. The Pecking Order of Free Radicals and Antioxidants: Lipid Peroxidation, α-Tocopherol, and Ascorbate. *Arch. Biochem. Biophys.* **1993**, *300* (2), 535−543.
(95) Kawanishi, S.; Inoue, S.; Yamamoto, K. Hydroxyl radical and singlet oxygen production and DNA damage induced by carcinogenic metal compounds and hydrogen peroxide. *Biol. Trace Elem. Res.* **1989**, *21*, 367−372.
(96) Wang, Y.; Tang, T.; Yuan, Y.; Li, N.; Wang, X.; Guan, J. Copper and Copper Complexes in Tumor Therapy. *ChemMedChem.* **2024**, No. e202400060.
(97) Lee, S. Y. Temozolomide resistance in glioblastoma multiforme. *Genes Dis.* **2016**, *3* (3), 198−210.
(98) Chen, X. Y.; Zhang, M. J.; Gan, H. Y.; Wang, H. P.; Lee, J. H.; Fang, D.; Kitange, G. J.; He, L. H.; Hu, Z.; Parney, I. F.; Meyer, F. B.; Giannini, C.; Sarkaria, J. N.; Zhang, Z. G. A novel enhancer regulates MGMT expression and promotes Temozolomide resistance in glioblastoma. *Nat. Commun.* **2018**, *9*, 2949.
(99) Jiapaer, S.; Furuta, T.; Tanaka, S.; Kitabayashi, T.; Nakada, M. Potential Strategies Overcoming the Temozolomide Resistance for Glioblastoma. *Neurol. Med. Chir.* **2018**, *58* (10), 405−421.
(100) Kitange, G. J.; Carlson, B. L.; Schroeder, M. A.; Grogan, P. T.; Lamont, J. D.; Decker, P. A.; Wu, W. T.; James, C. D.; Sarkaria, J. N. Induction of MGMT expression is associated with Temozolomide resistance in glioblastoma xenografts. *Neuro-Oncology* **2009**, *11* (3), 281−291.
(101) Agrawal, K.; Asthana, S.; Kumar, D. Role of Oxidative Stress in Metabolic Reprogramming of Brain Cancer. *Cancers* **2023**, *15* (20), 4920.
(102) *CrysAlisPro Versions 1.171.42.49 (Rigaku Oxford Diffraction)*, 2022.
(103) Sheldrick, G. M. SHELXT - Integrated space-group and crystal-structure determination. *Acta Crystallogr., Sect. A: Found. Adv.* **2015**, *A71*, 3−8.
(104) Sheldrick, G. M. Crystal structure refinement with SHELXL. *Acta Crystallogr. Sect. C Struct. Chem.* **2015**, *C71*, 3−8.
(105) Dolomanov, O. V.; Bourhis, L. J.; Gildea, R. J.; Howard, J. A. K.; Puschmann, H. OLEX2: a complete structure solution, refinement and analysis program. *J. Appl. Crystallogr.* **2009**, *42* (2), 339−341.
(106) Moulder, J. F.; Stickle, W. F.; Sobol, P. E.; Bomben, K. D. *Handbook of X-Ray Photoelectron Spectroscopy*; Perkin-Elmer Corporation: Eden Prairie, 1996.

https://doi.org/10.1021/acs.jmedchem.4c00821
J. Med. Chem. XXXX, XXX, XXX−XXX